Monthly Notices of the ROYAL ASTRONOMICAL SOCIETY

MNRAS **549,** 1–25 (2026)
Advance Access publication 2026 June 2

https://doi.org/10.1093/mnras/stag1028

ATLAS100 – I. A volume-limited sample of supernovae and related transients within 100 Mpc

S. Srivastav [1,2]★ S. J. Smartt [1,2] T. Moore [2,3] K. W. Smith [1,2] D. R. Young [2] M. D. Fulton [2] C. R. Angus [2] M. Nicholl [2] H. F. Stevance [1] T.-W. Chen [4] A. Pastorello [5] J. Sommer [6] F. Stoppa [1] J. W. Tweddle [1] J. P. Anderson [7] M. E. Huber [8] A. Rest [3,9] L. Rhodes [10,11] L. J. Shingles [2,12] A. Aamer [2,13] A. Clocchiatti [14,15] A. J. Cooper [1] N. Erasmus [16,17] J. H. Gillanders [1] D. Magill [2] G. Pignata [18] P. Ramsden [2,19] B. P. Schmidt [20] X. Sheng [2] J. G. Weston [2] L. Denneau [8] and J. L. Tonry [8]

Affiliations are listed at the end of the paper

Accepted 2026 May 25. Received 2026 May 13; in original form 2026 February 24

ABSTRACT

We present ATLAS100 – a sample of 1729 supernovae and other explosive optical transients within ∼100 Mpc observed by the ATLAS survey over a span of 5.75 yr from 2017 September 21 to 2023 June 21. The volume-limited sample includes transients associated with galaxies with a spectroscopic redshift of $z \leq 0.025$, and spectroscopically classified transients within this redshift threshold where a host redshift was not available in existing catalogues. Our host galaxy list is constructed from aggregating all available galaxy redshift and distance catalogues. We carefully select all transients within a projected radius of 50 kpc of these hosts. The ATLAS100 transient sample has a host galaxy redshift completeness fraction of 83 per cent, consistent with expectations for the redshift completeness of local galaxy catalogues. Within this volume, the spectroscopic classifications are 87 per cent complete and we reclassify many ambiguous transients with joint light curve and spectroscopic considerations. Here, we release the catalogue together with compiled, binned, and cleaned ATLAS photometry for all transients. We fit the light curve data to derive peak luminosities and characteristic time-scales. We explore the sample characteristics, demographics, and discuss the completeness and purity of the sample. This is the first in a series of papers that will explore the rates and physical parameters of a complete and large sample of nearby supernovae and transients brighter than $M \lesssim -16$.

Key words: surveys – catalogues – supernovae: general – transients: supernovae.

1 INTRODUCTION

The advent of modern robotic wide-field optical sky surveys, coupled with advances in detector technology and software techniques, has revolutionized the study of supernovae (SNe) and other transient phenomena. The All-Sky Automated Survey for Supernovae (ASAS-SN; B. J. Shappee et al. 2014) has been capable of covering the entire visible sky rapidly at a sensitivity of $m \lesssim 17.5$ mag. Larger aperture facilities such as the Catalina Real-time Transient Survey (CRTS; A. J. Drake et al. 2009), Palomar Transient Factory (PTF; N. M. Law et al. 2009; A. Rau et al. 2009), Panoramic Survey Telescope and Rapid Response System or Pan-STARRS1 (PS1; N. Kaiser et al. 2010; K. C. Chambers et al. 2016), the La Silla Quest (LSQ; C. Baltay et al. 2013) and the BlackGEM telescope array (P. J. Groot et al. 2024) with footprints of ∼10 deg^2, have surveyed sky areas of a few thousand square degrees with a cadence of a few days. The Asteroid Terrestrial-impact Last Alert System (ATLAS; J. L. Tonry et al. 2018), Zwicky Transient Facility (ZTF; E. C. Bellm et al. 2019), and the Gravitational-wave Optical Transient Observer (GOTO; D. Steeghs et al. 2022) have extended the footprints to ∼50–100 deg^2, maintaining good sensitivity ($m \lesssim 20$) with enhanced cadence all-sky capability. Additionally, dedicated spectroscopic facilities for classification and follow-up, such as the Public ESO Spectroscopic Survey for Transient Objects (PESSTO and its extensions; S. J. Smartt et al. 2015), the Spectral Energy Distribution Machine (SEDM; N. Blagorodnova et al. 2018) among others, have contributed immensely to the discovery and characterization of novel and exotic transient sub-classes (A. Gal-Yam 2017; M. Modjaz, C. P. Gutiérrez & I. Arcavi 2019), revealing new and hitherto uncharted regions in the duration–luminosity phase space (M. M. Kasliwal 2012).

Rapidly evolving transients (RETs) with characteristic time-scales of $\lesssim 10$ d have been identified previously in surveys including Pan-STARRS1 (M. R. Drout et al. 2014), PTF, and Supernova Legacy Survey (I. Arcavi et al. 2016), Dark Energy Survey (M. Pursiainen et al. 2018), and ZTF (A. Y. Q. Ho et al. 2023). RETs comprise a heterogeneous family of transients that include luminous

★ E-mail: shubham.srivastav@physics.ox.ac.uk

fast blue optical transients (LFBOTs; S. J. Prentice et al. 2018), the interaction-driven sub-classes of Ibn and Icn SNe (C. Pellegrino et al. 2022a), the mysterious luminous fast coolers (LFCs; M. Nicholl et al. 2023) found in elliptical host galaxies and the faint, fast, and elusive class of kilonovae resulting from binary neutron star mergers (B. P. Abbott et al. 2017). The low luminosity region in the duration–luminosity diagram has been increasingly populated by a colourful variety of 'gap' transients with peak luminosities intermediate to traditional SN classes and nova eruptions ($-10 \gtrsim M \gtrsim -16$). These include luminous red novae (LRNe; N. Blagorodnova et al. 2017), intermediate luminosity red transients (ILRTs; Y. Z. Cai et al. 2021), and luminous blue variables (LBVs; N. Smith et al. 2011b). The narrow line emission and optical faintness of these transients often mean their low signal-to-noise and low-resolution spectra remain ambiguous. Calcium-strong transients (CaSTs; H. B. Perets et al. 2010) comprise another family of faint and fast transients, with a preference for early-type hosts and remote locations (K. J. Shen, E. Quataert & R. Pakmor 2019). Type Iax SNe constitute a peculiar low-velocity and low-luminosity sub-class of thermonuclear SNe Ia (R. J. Foley et al. 2013) thought to arise from pure deflagrations (F. Lach et al. 2022) in carbon–oxygen white dwarfs (WDs). Faint SNe Iax ($M \gtrsim -16$) occupy a similar region as other gap transients, with the most extreme observed events being up to 6 magnitudes fainter than normal SNe Ia at peak, synthesizing merely a few 10^{-3} $M_\odot$ of radioactive ^{56}Ni (e.g. R. J. Foley et al. 2009; S. Valenti et al. 2009; M. D. Stritzinger et al. 2014; S. Srivastav et al. 2020a; V. R. Karambelkar et al. 2021; L. A. Kwok et al. 2025; E. A. Zimmerman et al. 2026). These faint transients are only discovered in the nearby Universe, which means all-sky surveys are required to maximize the search volume.

At the other extreme of the duration–luminosity phase space, superluminous SNe (SLSNe; R. M. Quimby et al. 2011) constitute the most energetic and powerful explosions in the Universe. Tidal disruption events (TDEs; see B. Mockler et al. 2025, for a recent review) comprise a class of luminous nuclear transients (NTs) resulting from the disruption of a star that strays within the tidal radius of a massive black hole (MBH). TDEs emit across the electromagnetic spectrum from X-rays to radio (S. Gezari 2021), and this emission can be used to independently decipher the properties and demographics of MBHs in otherwise dormant environments.

In addition to the discovery of new transient classes, recent surveys have also enhanced our understanding of the diversity within existing SN (sub)classes. These include the zoo of thermonuclear SNe (S. Taubenberger 2017), stripped-envelope SNe (SESNe) with double-peaked light curves (e.g. H. Kuncarayakti et al. 2023; C. R. Angus et al. 2024; Y. Sharma et al. 2024), and interacting transients with precursor emission from months to years preceding explosion (e.g. A. Pastorello et al. 2013; E. O. Ofek et al. 2014; Y. Dong et al. 2024; S. J. Brennan et al. 2025). These surveys also enable the study of large and homogeneous samples of SNe, vital for investigating the demographics, luminosity functions, and volumetric rates for different SN types and sub-types. The Lick Observatory Supernova Search (LOSS; W. Li et al. 2011) has been the benchmark for local Universe SN rates for over a decade, informing studies of progenitor channels (N. Smith et al. 2011a). This was based on observing targets from galaxy catalogues, followed by measured rates from wide-field surveys with no input galaxy bias. Determining SN rates in the local Universe is advantageous as the follow-up observational data (spectra and light curves) are of higher quality and inexpensive (in terms of telescope time) for the bright sources compared to higher redshift surveys (M. T. Botticella et al. 2017; P. Wiseman et al. 2021). The challenge is covering sufficient sky area to map the volume, which was achieved by ASAS-SN for different SN Ia subclasses (P. Chen et al. 2022; D. D. Desai et al. 2024, 2026) and SN II sub-classes (T. Pessi et al. 2025), and by PTF for volumetric rates of normal SNe Ia and CaSTs (C. Frohmaier et al. 2018, 2019). The ZTF bright transient survey (BTS; C. Fremling et al. 2020; D. A. Perley et al. 2020) provides a powerful magnitude-limited sample, leading to rates. The ZTF census of the local universe (CLU; K. De et al. 2020), and now the ongoing complete astronomical transient survey (CATS150; K. K. Das et al. 2025b) are volume-limited surveys aiming to classify all transients within 150 Mpc.

The ATLAS project was designed and funded by NASA to discover near-earth objects (NEOs) and potentially hazardous asteroids or PHAs (J. L. Tonry 2011; J. L. Tonry et al. 2018; A. N. Heinze et al. 2021), through an all-sky survey system. The primary mission of mapping our neighbourhood in the Solar system has been successful with the discovery of 1330 NEOs, 113 PHAs, and 111 comets,[1] including the potential impactor 2024 YR4 (B. T. Bolin et al. 2025) and only the third interstellar object, comet C/2025 N1 or 3I/ATLAS (D. Z. Seligman et al. 2025). The 1−2 d, all-sky cadence is a rich resource for stellar astrophysics (A. N. Heinze et al. 2018) and extragalactic transients. As described by K. W. Smith et al. (2020), the ATLAS project continually processes the nightly data for extragalactic transients, releasing the discoveries immediately through the International Astronomical Union's Transient Name Server (TNS). With the discovery of AT 2018cow, ATLAS revealed the class of LFBOTs for the first time (S. J. Prentice et al. 2018; S. J. Smartt et al. 2018). ATLAS also discovered the first optical counterpart of an extragalactic fast X-ray transient (FXT) from the Einstein Probe (J. H. Gillanders et al. 2024), and the best candidate for a pair-instability supernova (SN 2018ibb; S. Schulze et al. 2024). ATLAS routinely covers the skymaps of LIGO–Virgo–KAGRA gravitational wave detections to search for electromagnetic counterparts (B. Stalder et al. 2017; K. Ackley et al. 2020; S. J. Smartt et al. 2024). With over 23 000 SN candidates registered on the TNS and over 5000 spectroscopically classified (as of January 2026), ATLAS is now a rich source for SN population studies (e.g. S. Srivastav et al. 2022; B. Ayala et al. 2025; K. Ertini et al. 2026), and provides open public access to light curves of any celestial source (L. Shingles et al. 2021).

Sampling the population of extragalactic transients within a fixed volume of the Universe provides an observational sample for direct comparison with theoretical stellar population and evolution studies. Biases that exist in magnitude-limited studies are mitigated but not removed completely. With the goal of sampling all transients within a fixed volume, in this paper we introduce ATLAS100, a volume-limited sample of transients within a redshift of $z \leq 0.025$ ($D \lesssim 100$ Mpc) detected by the ATLAS survey over nearly 6 yr of operation during 2017 September 21 to 2023 June 21. The sample features more than 1700 transients, of which ~ 40 per cent were discovered by ATLAS. The remaining 60 per cent were discovered and reported first to the TNS by other surveys but were detected independently by ATLAS. The full catalogue and calibrated, cleaned ATLAS light curves of all transients in the sample are publicly released with this paper. This is the first in a series of papers that will constrain the SN population within this volume with high statistical significance, lack of host galaxy

[1] https://atlas.fallingstar.com; as of 2026 February 5.

bias, having well measured light curves and good spectroscopic completeness.

2 ATLAS100 SAMPLE DEFINITION

2.1 ATLAS survey

ATLAS was designed as an all-sky, high-cadence survey, comprising multisite, coordinated, wide-field telescopes, with two each in the Northern and Southern hemispheres. The project began a 2-d cadence northern sky survey (above $\delta = -50^\circ$) with the two units in Hawaii in January 2017.[2] The addition of the two southern units in Sutherland (South Africa) and El Sauce (Chile) in 2022 brought all-sky coverage with a 1-d cadence (weather permitting at all sites).[3]

As described in detail by J. L. Tonry et al. (2018), each unit has a 5.375° square detector at the focal plane of a 'Wright Schmidt' telescope with an effective aperture of 0.5 m. This provides a 28.9 deg^2 field of view, with typical 5σ limiting AB magnitudes of 18.5−19.5 mag for a 30 s exposure (depending on sky conditions). Images are obtained in two broad-band filters – cyan (c) and orange (o), roughly equivalent to a composite $g + r$ and $r + i$, respectively. The real-time data processing for stationary transients have been described by K. W. Smith et al. (2020). Difference imaging is performed for the data from each ATLAS unit and all positive sources of 5σ significance are catalogued and processed by the ATLAS transient science server. Typically, ATLAS observes a camera footprint 4 times within 40−60 min, with the images separated by a temporal gap to optimize the successful linking of NEO detections and construction of tracklets. For stationary transients, we require at least three quality detections ($> 5\sigma$ significance) within a 24 h time period, defined by an integer whole MJD, to create an object that will then be assessed further. A convolutional neural network has been trained on human-verified real transients and known slow-moving objects (point sources in 30 s exposures) for real-bogus classification (K. W. Smith et al. 2020). Further refinements were made to the convolutional neural network described by J. G. Weston et al. (2024), but these changes were made after the sample definition window. In 2025, ATLAS introduced the Virtual Research Assistant (VRA) to significantly improve the selection of real, astrophysical transients (H. F. Stevance et al. 2025), in an effort to reduce the workload on human scanners. The VRA is currently in operation as we continue the ATLAS100 survey, but did not play a role in the sample selection process for this paper. Access to the full history of ATLAS photometry at any point on the sky is publicly available through the forced photometry server (L. Shingles et al. 2021), linked from the ATLAS home page.[4]

2.2 Sample definition

The ATLAS100 sample aims to map a complete population of SNe and other extragalactic transients within a distance of $\lesssim 100$ Mpc. The time window for this sample covers a period of 5.75 yr, spanning 2017 September 21 (MJD 58017) to 2023 June 21 (MJD 60116). The corresponding redshift for a luminosity distance of $D_{\rm L} \sim 100$ Mpc depends on the assumed value of the Hubble constant H_0. We chose a redshift threshold of $z \leq 0.025$, which corresponds to a distance limit of $D_{\rm L} \approx 109$ Mpc assuming $H_0 = 70\,{\rm km\,s^{-1}\,Mpc^{-1}}$ and a flat cosmology with $\Omega_{\rm M} = 0.3$. This redshift/distance limit was chosen for several reasons. Within this volume, there is approximately 1 SN per day discovered, which over several years provides a significant statistical sample. The ATLAS sensitivity in the o band (most frequently deployed) of $m_o \approx 19.0 \pm 0.5$ corresponds to $M_o \approx -16 \pm 0.5 - A_o$ at 100 Mpc, where A_o is the combined Milky Way (MW) and internal host galaxy extinction. For low values of extinction, this absolute magnitude will detect SNe Ia ≈ 3 mag before peak at 100 Mpc (typically 2 weeks before maximum), and $M_o = -15.9$ is the peak measured magnitude of the kilonova AT 2017gfo (average of r and i bands at +0.7 to +0.9 d post-merger; I. Andreoni et al. 2017; S. J. Smartt et al. 2017). Fig. 1 illustrates the completeness limit for $m_o \lesssim 19.0 \pm 0.5$ as a function of distance for $M_o = -15.9$ (appropriate for AT 2017gfo) and $M_o = -14$, which corresponds to one of the faintest known SN Iax 2019gsc (S. Srivastav et al. 2020a). The absolute magnitudes of $M_o = -14$ and -16 also correspond to a normal SN Ia at 5 and 3 mag before peak, at phases of roughly -16 and -14 d relative to maximum, respectively.

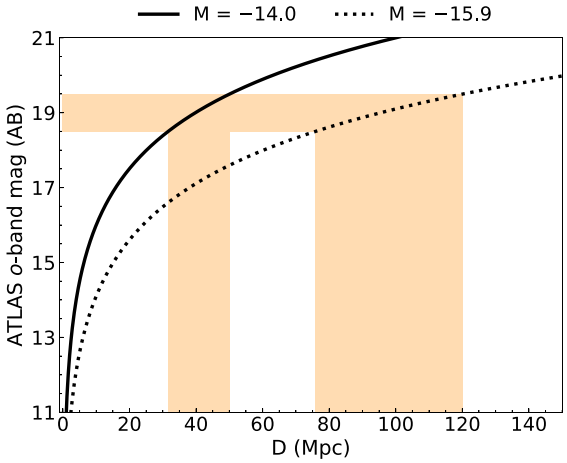

Figure 1. The o band magnitude versus distance for transients with absolute magnitudes $M_o = -14$ and $M_o = -15.9$. The shaded regions project the sensitivity of $m_o = 19.0 \pm 0.5$ to the distance to which a source would be detected.

The ability to find young, rapidly rising transients as opposed to those only within a few days of peak, at greater distances, was another motivation for choosing 100 Mpc as the distance limit. We have been monitoring every transient ATLAS finds within 100 Mpc in real time, due to the scientific promise of finding rare and intrinsically faint transients, or very young SNe. Since 2019 we have been alerting the community through AstroNotes for every transient within 100 Mpc discovered by ATLAS with robust pre-discovery non-detections (e.g. K. W. Smith et al. 2019) to encourage spectroscopic classification and further follow-up observations. We released 350+ AstroNotes from 2019 until June 2023. We also conducted programmes to classify these nearby ATLAS transients at the 3.6 m NTT, first through the ePESSTO campaign (S. J. Smartt et al. 2015) and then through the ePESSTO+ consortium (C. Inserra 2023), alongside access to the 2 m Liverpool Telescope (LT; I. A. Steele et al. 2004). The PESSTO surveys classified

[2]The first ATLAS unit at Haleakala was operational from 2015, with Mauna Loa commissioned in 2017.
[3]In July 2025, a fifth ATLAS unit in Tenerife (Spain) with a different optical and detector design came into operation. This unit was not used in the sample presented in this paper.
[4]https://fallingstar-data.com/forcedphot/

261 of the 1502 classified transients in the sample (17.4 per cent), behind only the ZTF group that accounted for 491 classifications (32.7 per cent).

Our initial selection of the ATLAS100 sample, both during the operational phase of the 2017–2023 survey and in retrospective checks, is based primarily on cross-matching transients with host-galaxy catalogues. This provides a secure host redshift, but we also supplement this with transients that lack a host redshift but have a spectroscopic redshift that places them within $z \leq 0.025$. These were public spectroscopic classifications on the TNS, where the redshift of the transient (TNS object z) was within our threshold of 0.025. In such cases, the TNS object redshift is usually inferred from spectral template matching tools such as SUPERFIT (D. A. Howell et al. 2005), SuperNova IDentification (SNID; S. Blondin & J. L. Tonry 2007), GELATO (A. H. Harutyunyan et al. 2008), or DASH (D. Muthukrishna, D. Parkinson & B. E. Tucker 2019). These redshifts are generally reported to two decimal places and are not as reliable as spectroscopic host redshifts, mostly due to the width of the spectral features and degeneracy between redshift, SN phase, and ejecta expansion velocity. Occasionally, the classification spectra show narrow emission lines from the host, providing a secure redshift. A sub-set of this volume-limited sample was described by S. Srivastav et al. (2022), where it was used to constrain the volumetric rates of SNe Iax.

We use the SHERLOCK[5] (D. R. Young 2023) PYTHON package and its supporting backend data base to assign a contextual classification to all candidate static transients in the ATLAS data stream. Sherlock achieves these classifications by mining an extensive library of archival catalogues of known astrophysical sources. These catalogues are hosted in a 4.5 TB MySQL data base, indexed by sky-location using the Hierarchical Triangular Mesh (HTM) indexing scheme. The catalogues include most of the major historical and ongoing astronomical surveys, including *Gaia* DR3 (Gaia Collaboration 2023), Sloan Digital Sky Survey or SDSS DR12 (S. Alam et al. 2015), Pan-STARRS1 Science Consortium surveys (K. C. Chambers et al. 2016; H. A. Flewelling et al. 2020; E. A. Magnier et al. 2020), and Two Micron All Sky Survey or 2MASS (M. F. Skrutskie et al. 2006). The SHERLOCK data base also hosts many curated, source-specific catalogues, including the NED-D catalogue of galaxies and the Local AGN Survey (LASr; D. Asmus et al. 2020) catalogue. Finally, SHERLOCK can dynamically query and cache data from the NASA Extragalactic Database (NED). Many of these catalogues report measured spectroscopic redshifts and/or redshift-independent distance measurements of the extragalactic sources they contain. Fig. 2 shows a histogram representing the major catalogues for the host galaxies in ATLAS100 cross-matched by SHERLOCK. NED and LASr serve as the primary sources for spectroscopic host galaxy redshifts for the transients in this sample.

SHERLOCK employs intelligent cross-matching of these catalogues and a decision-tree algorithm to predict the nature of each transient based on their cross-matched associations. The contextual classification returned by SHERLOCK is described in more detail by K. W. Smith et al. (2020), and can include 'VS' (variable star), 'AGN' (if transient source is coincident with known and catalogued Active Galactic Nuclei or AGN), 'SN' (likely to be a supernova based on association with a catalogued galaxy), and 'NT' (nuclear transient, coincident with the core of a galaxy that is not a known AGN). During ATLAS survey operations, the contextual

[5]https://github.com/thespacedoctor/sherlock

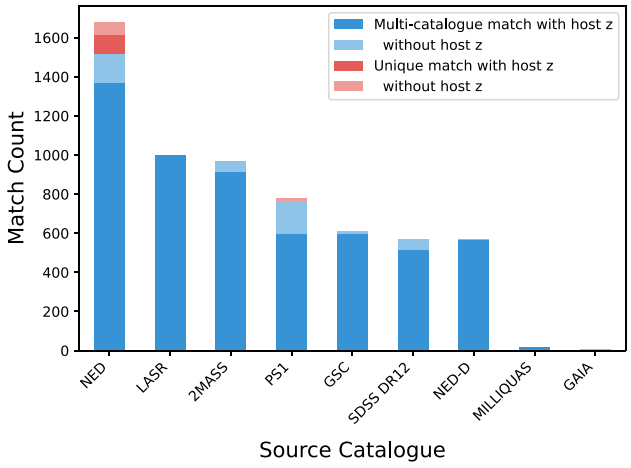

Figure 2. Histogram showing the number of matches to different source catalogues mined by SHERLOCK for the host galaxies of 1729 transients in ATLAS100.

classifications from SHERLOCK are assigned automatically, and transients are promoted to a dedicated data base table for manual review. These are the first targets that the on-duty team checks every day.

For this summary paper, we compiled an initial list of all potential transients detected by ATLAS within ∼100 Mpc. This list includes transients identified by SHERLOCK as associated with a host galaxy with $z \leq 0.025$ or directly measured median distance $D \leq 100$ Mpc on NED, or with TNS Object $z \leq 0.025$. A projected radial distance of 50 kpc was assumed by SHERLOCK as the maximum radius of association for galaxies with known redshifts. Transients that are more than 50 kpc from their likely host have been identified (e.g. K. Maguire et al. 2011, at ≥150 kpc), but these are rare and the hosts are not confidently associated with the SN. The most common sub-class of transients with large offsets are CaSTs, which have been found between 10 and 45 kpc from their most likely hosts (J. D. Lyman et al. 2014). Each object in this preliminary list was carefully examined manually, including the image stamps, SHERLOCK host association, the classification spectrum on TNS (if available), and if the reported redshift on TNS was consistent with the SHERLOCK host redshift (if available). Once a host galaxy association was established, we adopted the redshift of the identified host galaxy (from NED) as the redshift of the transient for further analysis. If a spectroscopic host redshift was not available, then the redshift derived from the classification report on TNS was adopted.

The preliminary list of transients compiled following the criteria defined above was subjected to a careful vetting process to identify and eliminate contaminants, described below.

2.3 Sample vetting and rejection of contaminants

The following categories of contaminants were identified and rejected in our vetting process:

(i) *Novae and nova candidates*. We do not include extragalactic novae in our sample, which is restricted to SNe and other extragalactic transients such as TDEs, CaSTs, and other gap transients. We therefore rejected confirmed novae with a spectroscopic classification on TNS, or identified as such through Astronomer's Telegrams (ATels). We also removed nova candidates, which we identify as unclassified transients in nearby host galaxies with a

peak absolute magnitude $M \lesssim -9$ that were likely novae. At this absolute magnitude, novae are detected only in galaxies within 3−4 Mpc, with M31 and Centaurus A being good examples where we have uncovered multiple nova candidates. A total of nine candidate novae were identified and removed from the sample. We note, however, that we may have rejected unclassified, nearby, and faint gap transients such as LBV eruptions and LRNe. Of the nova candidates that were removed, we highlight AT 2022kjj in M31, that shows a long-duration, undulating light curve. This transient does not look like a typical nova, and could be a gap transient in M31.

(ii) *Cataclysmic Variables (CVs) and CV candidates*. Our preliminary extraction of $z \leq 0.025$ transients included several classified foreground CVs on the TNS with $z = 0$, these are common Galactic outbursts and were removed from the sample. A few unclassified candidates in our list were most likely foreground CVs, spatially coincident within the SHERLOCK cross-match radius of a 100 Mpc galaxy. Telltale signs of these objects in the light curve are a blue colour at peak, a short rise time (typically a few days) followed by immediate decline, and in some cases evidence of recurrent activity in ATLAS, ZTF, and/or PS1 history. A coincident, faint, blue stellar source was identified in PS1 reference images for some of these objects, corroborating their identification as foreground CVs. These were also removed from the sample. An example is AT 2020krl that was discovered by ATLAS with a projected separation of 18 kpc from the galaxy UGC 11 262 at $z = 0.019$, but was later classified as a foreground CV (L. Galbany et al. 2020).

(iii) *Background SNe*. The projected radial offset of 50 kpc was chosen to ensure we did not exclude SNe with large separations from their host (CCSNe and thermonuclear SNe can be found out to projected separations of ∼30 and ∼50 kpc, respectively, see Section 3.2). However, a 50 kpc radius circle projects to 1.7 arcmin at 100 Mpc, giving a sky search area of 9 arcmin^2, which is large enough that background contamination occurs. The size of the search radius is a compromise between purity and completeness and for our initial selection sifting we set the radius to a large value within SHERLOCK. For every transient, we visually inspected the multicolour reference images (Legacy Surveys, Pan-STARRS1, DSS, 2MASS, WISE) for any fainter host lying close to the transient that may be catalogued (with a photometric redshift) but lacks spectroscopic redshift or distance information. We flagged such transients as likely background contaminants, identified either during our day-to-day scanning process or during the final vetting stage for the preliminary sample. A total of 60 transients were identified during the survey period and removed as likely background sources. These are often confirmed as background SNe when a spectrum is obtained, but a majority of these are unclassified transients. For example, AT 2020bbl was cross-matched by SHERLOCK with the galaxy VV 457 ($z = 0.005$) at a projected separation of 7.9 kpc. However, the likely true host for this unclassified transient is a faint background galaxy (detected in Pan-STARRS 3π survey with $m_{r_{\rm Kron}} = 19.1$) that has a spectroscopic redshift, $z = 0.082$, from the Dark Energy Spectroscopic Instrument (DESI; DESI Collaboration 2024). SN 2020dul was similarly associated with NGC 5804 ($z = 0.014$) with a projected separation of 20.2 kpc, but was later classified as a background SN Ia at $z = 0.07$ (S. Srivastav et al. 2020b). No obvious faint host is visible for SN 2020dul; it appears hostless, but the spectroscopic redshift is secure.

There are therefore no background contaminants in the spectroscopically classified sample. We demonstrate in Section 3.2 that the offset distribution of the unclassified transients is comparable to the classified sub-sample. It is possible that despite our careful vetting, a small number of the unclassified sub-sample are background contaminants within the 50 kpc association radius of foreground $z \leq 0.025$ galaxies, and where the true host galaxy is too faint to be detected in archival images (see Section 3.2). Of the 60 transients that were rejected as likely background contaminants, we would expect no more than a few of these to have been misidentified and actually be transients lying within $z \leq 0.025$, based on both the high degree of spectroscopic completeness of local galaxy catalogues within 100−150 Mpc (S. R. Kulkarni, D. A. Perley & A. A. Miller 2018), and the unlikely combination of a faint transient occurring within a faint, ≤100 Mpc galaxy.

(iv) *Refined redshifts from host galaxy emission lines*. For ≈ 83 per cent of the transients in the sample, the adopted redshift is derived from the catalogued host galaxy from SHERLOCK. Thus, only a small fraction (≈ 17 per cent) of transients in the sample lacked prior host galaxy redshift information and where the transient redshift was inferred from the classification spectrum. For a sub-set of these transients that were classified through our programmes on LT or ePESSTO/ePESSTO+, we examined the two-dimensional (2D) spectra for signs of signal from the host galaxy. If host galaxy signals were present, we extracted the host spectrum and derived a more secure redshift from galaxy emission lines, primarily Hα, Hβ, and [O III] λ5007. In a few cases, the newly derived redshift from host emission features places the transient at $z > 0.025$; these were excluded from our sample. Examples include SN 2021adlt and SN 2021ubz. SN 2021adlt was classified by ePESSTO+ as an SN Ia at $z = 0.021$ based on a SNID comparison, however we derive a redshift of $z = 0.027$ from host emission features. SN 2021ubz was classified by ePESSTO+ as a 91T-like SN Ia at $z = 0.02$ using SNID. However, the ATLAS light curve would peak at $M_o \approx -18.7$ at that redshift, faint for the overluminous 91T-like Ia sub-class. We derive a redshift of $z = 0.030$ from the host galaxy emission lines instead, which implies a peak luminosity of $M_o \approx -19.6$, consistent with 91T-like SNe Ia. We note that this exercise was only carried out for the fraction of classification spectra where we have access to the raw 2D frames. These include 52 transients classified through either ePESSTO+ or our LT programme, out of 294 where a prior host galaxy redshift was not available. We note that this method favours redshift determination for late-type hosts.

(v) *Obvious misclassification*. During our vetting process, we also checked whether the ATLAS light curve shape and peak luminosity was roughly consistent with the reported spectral type on TNS. This is pertinent in particular for the 17 per cent of transients that did not have prior host galaxy redshift information. During this process, we identified a handful of obvious erroneous classifications where the reported redshift is inconsistent with the light curve properties. An example is SN 2017ili, classified as a normal SN Ia by ePESSTO (K. M. Lopez et al. 2017) at $z = 0.025$. At that redshift, the ATLAS light curve has a peak luminosity of $M_o \sim -15.5$, too faint for a normal SN Ia. A careful analysis using SNID shows good matches with SNe Ia at $z \sim 0.10-0.15$ instead, suggesting this is a background SN. Eight such identified events were also weeded out of the sample.

2.4 Spectral reclassification

During the vetting process, we examined the ATLAS light curve and the classification spectrum on TNS (where available) to ensure the reported spectral type and redshift (if derived from the classification spectrum) were broadly consistent with the light curve and luminosity. In a few cases, transients were classified through ATels but a classification report was not submitted to TNS. In other instances, the transient was classified on TNS but further follow-up observations (or published papers) conclusively show the transient belongs to a different spectral (sub)type. For example, some SNe IIP in ATLAS100 were reclassified as SNe IIb (or vice-versa) by detailed sample studies of SNe II observed by ATLAS (B. Ayala et al. 2025; K. Ertini et al. 2026); these were incorporated in our sample.

Finally, during the vetting process we encountered classifications where the spectral features, light curve, redshift, and/or host galaxy information were at odds with the reported spectral type on TNS. A full re-analysis of all available classification spectra was not performed for this study. Transients were reclassified only in the event of obvious misclassification, published ATels or papers, subsequent public light curve or spectroscopic information not available when the initial classification was reported to the TNS, or additional private follow-up data. The column labelled 'Spectral type' in the catalogue file (released with this paper) reflects the adopted spectral type for each transient in the ATLAS100 sample. The catalogue data table includes a flag for the source of the adopted spectral type for each transient. For most of the sample, the adopted spectral type in ATLAS100 matches the spectral type reported to the TNS. In a few cases where our adopted spectral type is different, the flag specifies the source for the adopted ATLAS100 spectral type – either from published literature or a reanalysis of publicly available data, or private communication based on unpublished follow-up data. The ATLAS100 adopted spectral type is different from the TNS spectral type for 67 transients (4.5 per cent of the classified sub-sample).

2.5 Light curve data products

We obtained ATLAS light curves for each SN in this sample using the publicly available ATCLEAN[6] package (S. Rest et al. 2023, 2025). With ATCLEAN we queried difference-image photometry from the ATLAS forced photometry (FP) server (L. Shingles et al. 2021) at the TNS reported position of each SN within a time window ranging from −500 to +1000 d since TNS discovery date (in the observer frame). The ATLAS FP data products were cleaned by ATCLEAN following S. Rest et al. (2025). We apply two quality control cuts to remove unreliable measurements using ATCLEAN default settings. We make an uncertainty cut to remove light curve points with large uncertainties with a threshold of $\sigma_F > 160$ μJy. The ATLAS FP server returns the point spread function fit reduced chi-squared statistic (χ^2_{PSF}) for each measured image. Any measurements with $\chi^2_{PSF} > 10$ were flagged as unreliable and removed. Finally, we bin the remaining measurements into nightly bins and adopt the 3σ-clipped average.

The light curve data release will generally include four data products for transients in ATLAS100. The data products include the cleaned and binned (1-d binning window) *o*-band and *c*-band data. For some transients, a baseline flux correction was applied to ensure the pre-explosion flux was consistent with zero. This offset was determined using a 200-d pre-explosion window, from −220 to −20 d relative to epoch of TNS discovery (more details in Appendix A). A baseline flux correction was applied for 275 light curves of 246 unique transients in ATLAS100 (out of 3449 light curves of 1729 unique transients). In case a correction was not required, the corrected data are just a copy of the uncorrected ATCLEAN output, but we include both data products for all transients for consistency. The light curve data are not corrected for any extinction along the line of sight.

For example, for SN 2019np, the binned *o*-band data from ATCLEAN is contained in the file named `2019np.o.1.00days.lc.txt`, while the baseline corrected data file is named `2019np.o.1.00days_zp_corr.lc.txt`. A similar naming structure is used for the *c*-band data. Table 1 shows an abridged version of the binned *o*-band light curve for SN 2019np.

Table 1. An abridged sample of ATLAS light curve data from ATCLEAN for one of the transients in ATLAS100. This table shows binned *o*-band light curve data for SN 2019np. The light curve data for all transients in ATLAS100 are publicly available as part of the ATLAS100 data release, the sample shown here is for guidance regarding its form and content.

MJD	uJy	duJy	Nclip	Ngood	m	dm
58493.55	520.4	7.6	0	4	17.109	0.016
58495.56	1393.5	6.2	2	8	16.040	0.005
58497.54	2836.0	8.6	1	7	15.268	0.003
58499.49	5112.0	30.0	0	1	14.629	0.006
58501.48	7508.1	20.0	1	3	14.211	0.003

2.6 Catalogue data products

The catalogue data are also made publicly available with the ATLAS100 data release (see Data Availability). The catalogue data include 40 columns; an abridged version is presented here for guidance (Table 2). The catalogue data include the coordinates of the transient and its identified host galaxy, adopted redshift (from its host galaxy if available, from the TNS object *z* if not), projected physical separation from the host, TNS discovery magnitude, and ATLAS peak magnitude.

3 RESULTS AND DISCUSSION

In this section, we present the general characteristics, statistics, and demographics of the ATLAS100 sample. This is followed by a discussion on the sample completeness and purity, and the key science outputs and highlights (ongoing and imminent) from the ATLAS100 sample.

3.1 Sample statistics and demographics

3.1.1 Redshifts and discovery magnitudes

The ATLAS100 sample consists of a total of 1729 transients that passed the vetting process described in Section 2.3. Fig. 3 shows the on-sky distribution of all the transients in the sample, generally tracing the distribution of nearby galaxies within 100 Mpc taken from LASr (D. Asmus et al. 2020). Since the southern ATLAS units in Chile and South Africa have been operational only since late 2021, the number of transients in the sample south of declination −50° (the limit of the northern Hawaiian units) are

[6] https://github.com/srest2021/atclean

Table 2. An abridged sample of the catalogue data accompanying the ATLAS100 data release. The catalogue data includes 40 columns, only nine are shown here due to space constraints.

ATLAS name	TNS name	RA (deg)	Dec. (deg)	Redshift	Spectral type	Host name	Angular sep (arcsec)	Physical sep (kpc)
ATLAS17lyk	2017hdz	30.281734	31.889047	0.017312	–	NGC 0783	26.87	9.46
ATLAS17koq	2017gmr	38.875728	−9.354185	0.005037	SN II	NGC 0988	34.87	2.7
ATLAS17mal	2017gvp	355.444951	−1.35088	0.022529	SN Ia	UGC 12 739	7.25	3.3
ATLAS17jvk	2017gpn	54.438205	72.532953	0.007388	SN IIb	NGC 1343	139.65	2.88
ATLAS17nan	2017hyf	32.387518	21.249009	0.017132	SN Ib	UGC 01652	8.85	3.08
ATLAS18ebi	2018ie	163.504332	−16.022679	0.014233	SN Ic-BL	NGC 3456	37.33	8.63
ATLAS18rso	2018ctv	21.466808	−1.367085	0.018086	SN Ia-91bg-like	NGC 0541	124.28	45.65
ATLAS18mkz	2017kam	205.682987	−24.335084	0.022496	SN II-pec	ESO 509− G 095	4.42	2.01
ATLAS18bcmc	2018aes	207.074017	3.945747	0.003906	ILRT	NGC 5300	31.69	3.12
ATLAS18qgb	2018bwo	3.507145	−23.193202	0.001558	LRN	NGC 0045	50.82	1.67

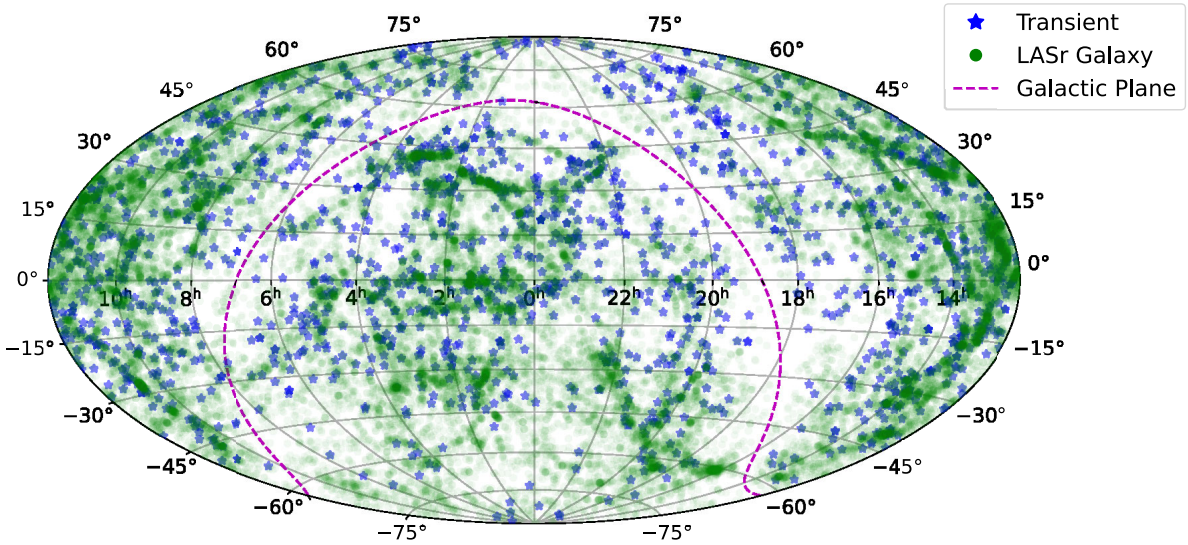

Figure 3. Sky distribution of the ATLAS100 transient sample. Also shown (green circles) is the distribution of local galaxies within 100 Mpc from the Local AGN Survey (LASr; D. Asmus et al. 2020).

much fewer. There are also fewer transients in the Galactic plane due to high levels of foreground extinction.

Fig. 4 shows the distribution of redshift and discovery magnitude (as reported to the TNS) for all transients in the ATLAS100 sample. The median redshift for the sample is 0.018 (0.006) and the median discovery magnitude reported to the TNS is 18.2 (1.2) mag, where the 1σ standard deviation is quoted in the brackets. We note that the discovery magnitudes are reported in different filters depending on the reporting survey (e.g. *o* or *c* band for ATLAS), and also sometimes reported in different photometric systems (e.g. Vega or AB). None the less the plot is still useful, and suggests a median absolute magnitude of −16.2 (1.4) mag at discovery for a typical transient given the median discovery magnitude and redshift for the sample. ATLAS-discovered transients in the sample (689 out of 1729) are shown as either orange or cyan circles, depending on whether the discovery filter was *o* or *c* band. At redshifts of $z = 0.010, 0.015, 0.020$, the effect of rounding the redshifts estimated from the spectra of the transients (lacking host galaxies) is visible as vertical overdensities. This indicates that even at $z \sim 0.01$, galaxy redshift catalogues are not complete, with SNe signposting the underlying hosts which are catalogued in imaging surveys but without measured redshifts.

Fig. 5 shows the distribution of the first ATLAS 5σ detection magnitude (top panel) and the peak ATLAS magnitude (bottom panel) for the classified and unclassified sub-sets, along with the complete ATLAS100 sample. These are observed magnitudes, not corrected for foreground Galactic or host galaxy extinction. The sub-set of classified events (87 per cent of the sample) is much larger, and thus a normalized histogram is shown for a meaningful comparison. Considering the sample (by definition) consists of the most nearby transients, a rather high fraction (13 per cent) is unclassified. It is therefore worth investigating if the sub-set of unclassified transients represents a distinct population. The median first ATLAS 5σ detection magnitudes are 18.06 (1.04) and 18.37 (0.93), for the classified and unclassified sub-sets, respectively. The median peak ATLAS magnitudes on the other hand are 17.12 (1.18) and 17.93 (0.94) for the classified and unclassified sub-sets, respectively. Although the difference is not significant, the peak ATLAS magnitudes suggest an overall fainter population for the unclassified events. The median redshift and median foreground Galactic extinction is identical for the two sub-sets, suggesting the difference in peak magnitude is not attributable to distance or MW extinction. We do not take host galaxy extinction into account here; however, we expect host galaxy extinction effects to average out given the large sample size.

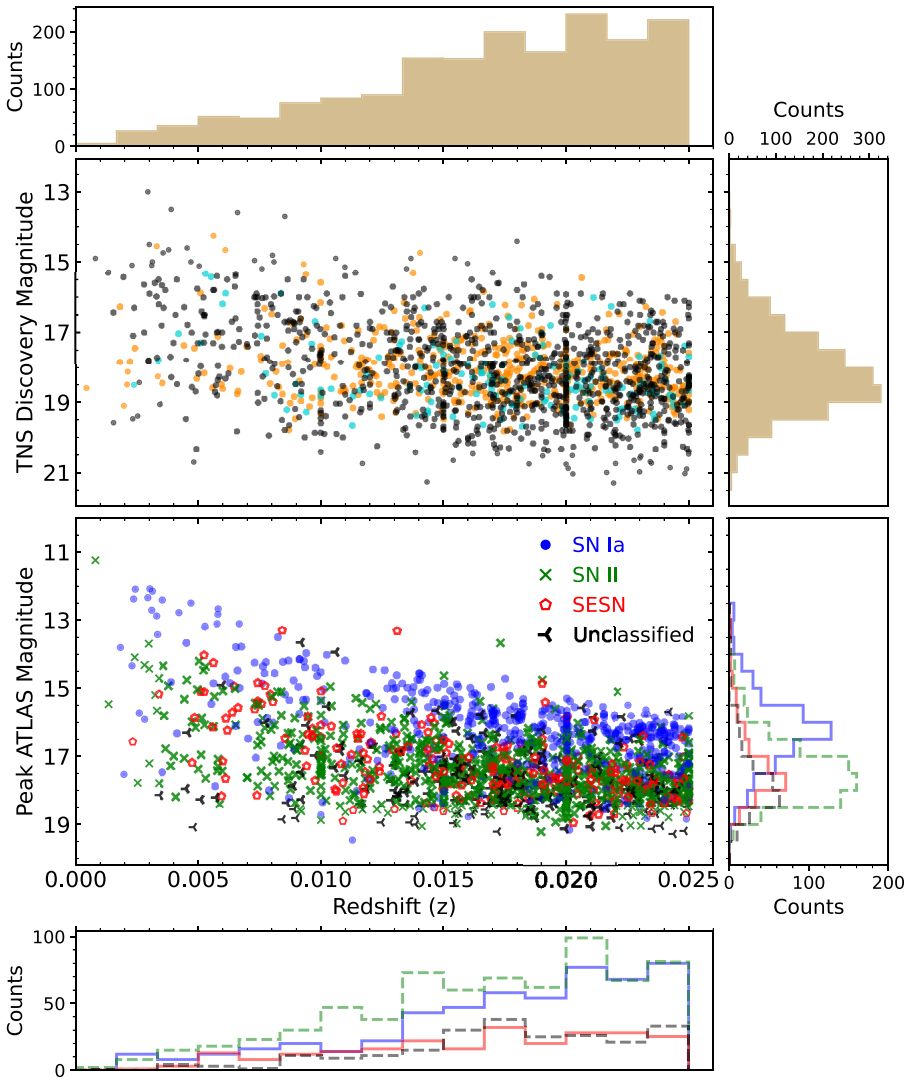

Figure 4. Upper panel: distribution of TNS discovery magnitude versus redshift for all transients in ATLAS100. The ATLAS discoveries (689 of the total 1729) are shown in either orange or cyan, depending on whether the discovery filter was *o* band or *c* band. Non-ATLAS discoveries are shown as black circles. The histograms for redshift and discovery magnitude are for the full sample, with bin widths of $\Delta z = 0.00167$ (corresponding to ∼7 Mpc) and Δmag = 0.5. Lower panel: distribution of peak observed ATLAS magnitude (without extinction correction) versus redshift, and the associated histograms for the key spectral types in the sample.

We also consider the possibility that the unclassified sub-set consists of a higher fraction of old SNe discovered after peak with declining light curves, emerging from solar conjunction. For old SNe discovered post maximum, the peak ATLAS magnitude (the same as the first ATLAS detection in this case) will be fainter than their true peak magnitude. These events are also less likely to be classified, since spectroscopic classification programmes generally prioritise young SNe with robust pre-discovery constraints for the explosion epoch. To test this, we checked the fraction of events within the classified and unclassified sub-samples that emerged from solar conjunction; i.e. with no pre-discovery non-detections within the last 30 d in their ATLAS forced photometry light curve (described in Section 2.5). 78 per cent of classified events have pre-discovery non-detections whereas the fraction is 72 per cent for unclassified events, suggesting that old SNe are not significantly overrepresented in the unclassified sub-set. This indicates that unclassified events in the ATLAS100 sample are broadly similar (albeit slightly fainter) to the population of classified SNe, rather than constituting a distinct sub-population of faint and/or fast transients. The spatial offsets of the unclassified sample (from their identified host) tend to follow the classified sample as discussed in Section 3.2, further supporting our assertion that these are not a physically different population than the classified sample.

3.1.2 *SN types and sub-types*

Table 3 lists a summary of the SN types and associated statistics and Fig. 6 shows the observed fractional representation of the key spectral types in the ATLAS100 sample. We stress that these are observed fractions that are not corrected for the intrinsic light curve shape and luminosity of the transient, survey coverage and variations in sensitivity, foreground Galactic extinction, galactocentric distance from the host, etc. They represent the raw data set from which rates can be determined. A detailed analysis pre-

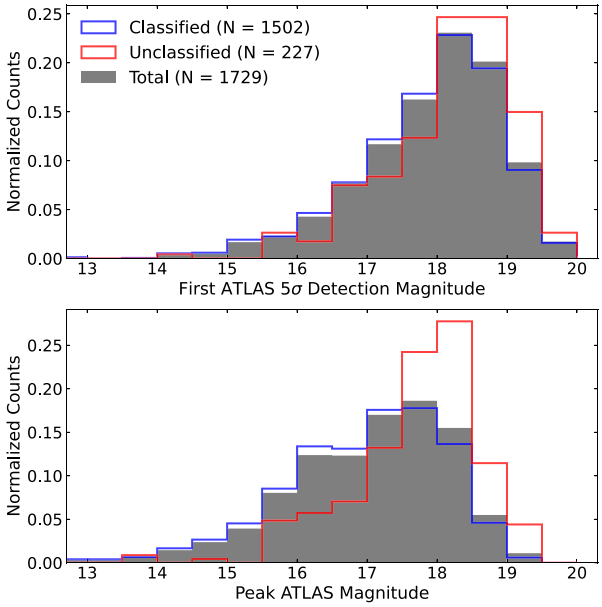

Figure 5. Upper panel: histogram of first ATLAS 5σ detection for the classified (blue) and unclassified (red) sub-samples. The full sample is shown in grey, and the *y*-axis is normalized to the total number of counts for a direct comparison. Lower panel: ATLAS peak magnitude for the classified and unclassified sub-samples. The bin width is 0.5 mag.

senting corrected volumetric rates and luminosity functions for different SN types and sub-types will be presented in future work.

Hydrogen-rich CCSNe or SNe II constitute the most abundant spectral type in the sample, comprising 40.0 per cent of the total sample and 46.1 per cent of the classified sub-sample. SESNe are relatively rare, comprising only 15.8 per cent of the classified events. CCSNe (SNe II + SESNe) account for ∼62 per cent of the classified sub-sample, whereas thermonuclear SNe Ia make up 35.4 per cent. The fraction of SNe Ia (of all sub-types), at 35.4 per cent of the classified subsample, is significantly higher than that found by LOSS in their volume-limited sample (24 per cent, within their 60 Mpc volume after corrections for completeness; W. Li et al. 2011). This is very likely due to the ATLAS completeness distance for the faintest CCSNe being lower than for the generally more luminous SNe Ia. This is evident in the histogram of redshift distribution as a function of spectral type (Fig. 4, lower panel). SNe Ia in the sample have a median redshift of 0.019, whereas SNe II are generally closer with a median redshift of 0.017. We confirm this by constructing a sub-sample within 60 Mpc ($z \lesssim 0.014$). This ATLAS60 sample comprises 471 transients, of which 121 are SNe Ia (25.7 per cent), consistent with LOSS.

SNe II in the sample are classified into one of the following sub-types on TNS: II-norm, IIP, IIn, and II-pec. Most of the objects classified as II-norm (just 'SN II' on TNS) are in fact SNe IIP based on the typical plateau in their light curves. However, full light curve information is usually not available when classification reports are submitted to the TNS, especially when the spectrum is obtained within a few days of explosion, as is increasingly the case for these nearby SNe. The category of II-norm will include both IIP and IIL (plateau and linear light curves), which can be distinguished further with ATLAS light curve data. SNe IIn are relatively rare, constituting 6.1 per cent of the observed SN II population and 4.5 per cent of the overall CCSN population in the sample, the latter being consistent with the corrected SN IIn

Table 3. Summary of the statistics, peak luminosities, and characteristic time-scales for the different spectral types in the ATLAS100 sample. $N_{\rm tot}$ is the total number of transients for a given spectral type and $f_{\rm tot}$ is the percentage of the 1502 total classified events. $N_{\rm cut}$ is the number of transients that passed the stringent light curve quality cuts (defined in Section 3.3) that were used to estimate the peak luminosity and duration. The median peak *o*-band magnitude and median duration is shown for all spectral sub-types with $N_{\rm cut} \geq 3$. The 1σ standard deviation in the peak absolute magnitude and duration is indicated in the brackets.

Spectral Type	$N_{\rm tot}$	$f_{\rm tot}$ (per cent)	$N_{\rm cut}$	Peak mag *o* band)	Duration (days)
Type II	**692**	**46.0**	**272**		
II-norm	643	42.8	251	−17.07 (0.74)	83.3 (28.7)
IIn	42	2.8	19	−17.81 (0.95)	64.8 (26.6)
II-pec	6	0.4	2		
Type Ia	**532**	**35.4**	**287**		
Ia-norm	467	31.1	248	−18.65 (0.55)	33.5 (5.5)
Ia-91bg	27	1.8	16	−17.65 (0.77)	20.6 (0.2)
Ia-91T	17	1.1	9	−19.01 (0.40)	40.5 (1.1)
Iax	14	0.9	9	−16.62 (1.29)	29.2 (3.1)
Ia-03fg	3	0.2	2		
Ia-02es	2	0.1	2		
Ia-CSM	1	0.1	0		
Ia-00cx	1	0.1	1		
SESN	**238**	**15.8**	**122**		
Ic	77	5.1	37	−17.18 (0.75)	29.3 (11.6)
Ib	72	4.8	44	−17.12 (0.43)	30.7 (6.3)
IIb	44	2.9	22	−17.27 (0.84)	28.7 (13.7)
Ib/c	16	1.1	6	−17.47 (0.25)	25.6 (3.0)
Ic-BL	13	0.9	4	−17.22 (0.65)	17.4 (6.8)
Ib/c-pec	9	0.6	5	−17.47 (0.15)	31.6 (7.1)
Ibn	7	0.5	4	−17.56 (0.30)	13.3 (2.6)
Icn	1	0.1	0		
Other	**40**	**2.7**	**13**		
LRN	12	0.8	2		
ILRT	11	0.7	5	−13.43 (0.83)	57.2 (18.7)
CaST	8	0.5	3	−16.30 (0.52)	24.8 (3.4)
TDE	4	0.3	2		
LBV	3	0.2	1		
AGN	1	0.1	0		
LFBOT	1	0.1	0		
Unclassified	**227**		**42**	−17.48 (1.22)	32.0 (32.6)
Total	**1729**		**736**		

to CCSN ratios from PTF and ZTF BTS (C. Cold & J. Hjorth 2023). Our observed SN IIn fraction is lower than the observed fraction in ZTF BTS by a factor of 2 (14.2 per cent of SNe II; D. A. Perley et al. 2020). Since SNe IIn are typically more luminous than normal SNe II, their observed fraction is higher in the magnitude-limited BTS sample. The ATLAS fraction of 6.1 per cent of all type II SNe is marginally lower than the 10.1 ± 3 per cent from LOSS (W. Li et al. 2011) but within the uncertainties.

There are six events that are classified as SN II-pec (0.9 per cent of SNe II). Most of these are either confirmed or likely 1987A-like SNe II characterized by a distinct long rise to maximum and lack of the usual plateau feature, such as SN 2021aatd (T. Szalai et al. 2024). 1987A-like events, thought to arise from blue supergiants, are rare and comprise a small fraction of SNe II (≈ 1.4 per cent; T. Sit et al. 2023). Our raw rates are even lower but have not yet been corrected for completeness within the volume.

The SESN sub-types present in our sample include all events with a root classification of SN IIb, Ib, SN Ic, or SN Ib/c. This

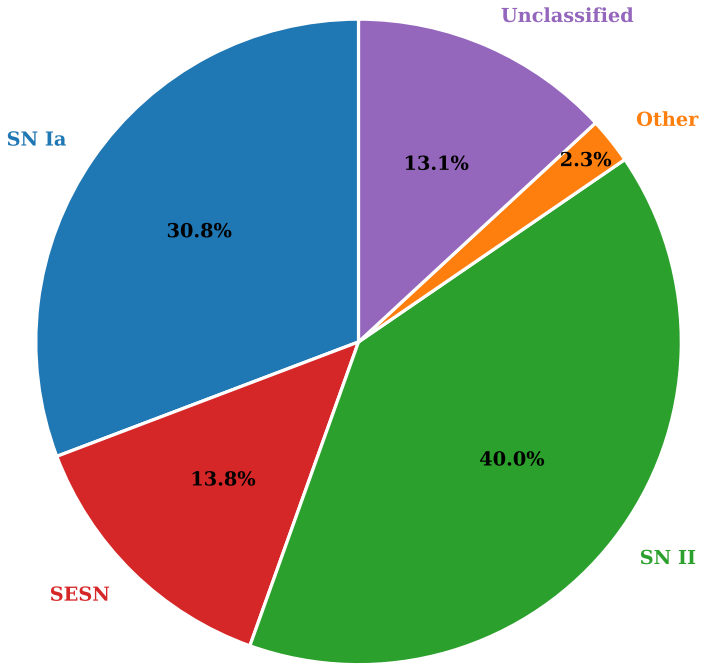

Figure 6. Spectroscopic classifications for the transients in ATLAS100.

includes Ibn, Icn, Ib-pec, Ic-pec, and broad-line Ic or Ic-BL. The SESN types represent those that are very likely the outcome of core-collapse in stars with $M_{\rm ZAMS} \gtrsim 8 M_{\odot}$. We do not include the class of transients that are often labelled as SN Ib-Ca-rich into this category as they likely originate from a different explosion mechanism. Ca-rich or alternatively Ca-strong transients (CaSTs; H. B. Perets et al. 2010) are placed into the 'Other' category, since despite their spectroscopic resemblance to SNe Ib at early times, the nature of their progenitors remains an enigma. For a significant fraction, the host environments are more compatible with a thermonuclear origin rather than core-collapse (K. J. Shen et al. 2019), although multiple progenitor channels have been suggested (K. De et al. 2020). This yields a total of 238 SESNe, accounting for 15.8 per cent of the classified sub-sample.

SNe Ia are further sub-divided into Ia-norm, Ia-91T, Ia-91bg, Ia-CSM, Ia-00cx, Ia-02es, and Ia-03fg, and Iax sub-types. An overwhelming majority (88 per cent) of SNe Ia in the sample belong to the Ia-norm category (i.e. classified as 'SN Ia' on TNS). However, most of these classifications are directly from the TNS (with the exception of either egregious misclassification or objects with published papers in the literature and hence a confirmed membership of a particular subtype), and a more careful analysis of the spectra combined with light curve analysis will likely reveal a higher fraction of peculiar SN Ia sub-classes in the sample (U. Burgaz et al. 2025). For instance, the ZTF SN Ia DR2 reported an observed fraction of 75 per cent for normal SNe Ia in their magnitude-limited sample (G. Dimitriadis et al. 2025), whilst also introducing a new sub-type dubbed Ia-18byg. We defer a more rigorous analysis for SNe Ia in this sample, including sub-classification, computation of intrinsic volumetric rates, and luminosity functions for the different Ia sub-types to a forthcoming paper.

Of the 532 SNe Ia in the sample, 17 are classified as Ia-91T (3.2 per cent), 27 as Ia-91bg (5.1 per cent), 14 as Iax (2.6 per cent). There is a small number of events belonging to rare sub-classes such as Ia-03fg (3), Ia-02es (2), Ia-CSM (1), and Ia-00cx (1). Here, we compare the observed fractions of Ia sub-types in ATLAS100 with the efficiency-corrected observed fractions from a volume-limited ($z < 0.06$) SN Ia sample from ZTF (U. Burgaz et al. 2025; G. Dimitriadis et al. 2025). The observed fraction of Ia-91T (3.2 per cent) in our sample is lower than the 12.2 per cent reported by ZTF (G. Dimitriadis et al. 2025). This is likely due to mistyping, suggesting a small fraction of SNe classified as Ia-norm on TNS belong to the overluminous Ia-99aa or Ia-91T sub-types. The observed fractions of Ia-91bg, and the rare sub-types of Ia-02es, Ia-03fg, and Ia-CSM in the sample are consistent with G. Dimitriadis et al. (2025). The fraction of Ia-CSM is consistent with the volumetric rate of $\lesssim 0.2$ per cent of the SN Ia rate (Y. Sharma et al. 2023).

SNe Iax are considered to be the most abundant peculiar sub-type of SNe Ia (S. W. Jha 2017). Based on a sub-set of the sample presented in this work, S. Srivastav et al. (2022) estimated a volumetric rate of 15^{+17}_{-9} per cent of the SN Ia rate. Furthermore, the Iax volumetric rate is expected to be dominated by faint events with $M_r \geq -16$ (S. Srivastav et al. 2022). The ATLAS100 sample is not complete at 100 Mpc for low-luminosity Iax events, with the faintest known object SN 2021fcg showing a peak luminosity of $M_r \sim -13$ (V. R. Karambelkar et al. 2021). It is thus unsurprising that the observed fraction of SNe Iax in the sample is lower than their intrinsic rates would suggest.

CCSNe and SNe Ia, together with the unclassified events, make up 97.7 per cent of the sample. Finally, we compare our observed fractions of the key spectral types of SNe II, SESN, and SNe Ia with an equivalent volume-limited version of the BTS sample. The latter is constructed by imposing $z \leq 0.025$ on the 5-yr BTS sample between 2018 May 1 and 2023 June 21. This volume-limited subsample of BTS contains 521 transients, all with a spectroscopic classification. The observed fractions in this BTS sub-sample are 43.0 per cent for SNe II, 32.2 per cent for SNe Ia and 16.9 per cent

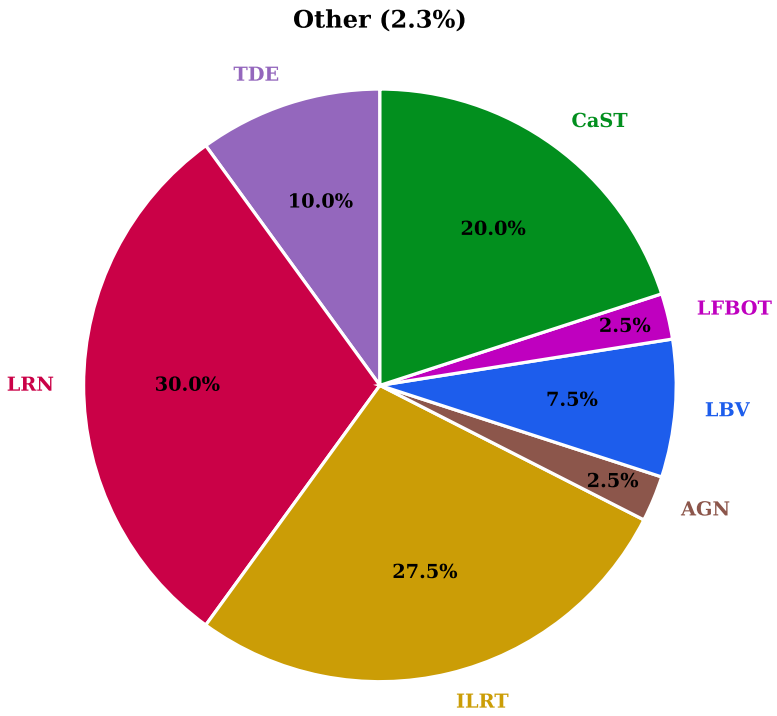

Figure 7. Spectroscopic classifications for the sub-set of transients labelled as 'Other' in Fig. 6.

for SESNe, comparable to the observed fractions in ATLAS100 (Table 3).

The remaining categories of transients are represented in the 'Other' category – these include 40 transients that include LBVs, LRNe, ILRTs, CaSTs, and TDEs. Fig. 7 shows the relative abundance of these rare transients in the ATLAS100 sample. Section 2.4 describes how transients in the sample were reclassified based either on reanalysis of public data, private follow-up data, or both. In particular, we reclassify a high fraction of gap transients (LBVs, ILRTs, LRNe) based on detailed follow-up data obtained for several individual events (private communication). For example, our reclassification increases the number of ILRTs in ATLAS100 from 8 to 11, and the number of LRNe from 6 to 12. Most of these reclassifications were at the expense of transients classified as either LBVs, or as 'Impostor-SN' on the TNS. The number of LBVs in the sample has diminished to three (from eight) after reclassification. In general, we note that LRNe and ILRTs are often misclassified as LBV eruptions. The three events classified on TNS as Impostor-SN are SN 2019fxy, SN 2020bfw, and SN 2022ryi. Their light curves indicate intermediate peak luminosities ranging from $-14 < M_o < -10$, and the classification spectra show blue continuua with prominent Balmer emission features. Based on the light curve, we reclassify SN 2019fxy as a likely ILRT. SN 2020bfw exhibits a long-lasting eruptive phase, and prominent He I emission in the classification spectrum (I. Irani et al. 2020). Based on these characteristics, we reclassify SN 2020bfw as a LBV. SN 2022ryi is reclassified as an LRN based on extensive follow-up data (private communication). After reclassification, LRNe (30.0 per cent), ILRTs (27.5 per cent), and CaSTs (20.0 per cent) constitute the bulk of these transients. It would appear that genuine giant outbursts from massive stars, often given the classification of LBV, are quite rare, and the bulk of these faint and intermediate luminosity gap transients are not from this type of massive star eruption. This requires further analysis of completeness within a smaller volume than 100 Mpc, and analysis of existing spectra and light curve data.

Besides these sub-types, there are also four TDEs within this 100 Mpc distance limit, implying a rate of roughly one optically bright TDE within 100 Mpc every 1.4 yr. The archetypal LFBOT AT 2018cow (S. J. Prentice et al. 2018; D. A. Perley et al. 2019) is also part of the sample, which was detected across the electromagnetic spectrum from hard X-rays to radio (A. Y. Q. Ho et al. 2019; R. Margutti et al. 2019). While other similar multi-wavelength emitting LFBOTs have been found (A. Y. Q. Ho et al. 2023), all are at significantly higher redshift indicating they are intrinsically rare by volume. Due to its uncertain physical nature, AT 2018cow was originally classified as Ic-BL on the TNS (and still remains so as of February 2026). However, it is now thought to be most likely a disruption event rather than a supernova (A. Inkenhaag et al. 2023).

There are two events in the sample classified as 'Galaxy' on the TNS (AT 2020wia and AT 2021aks). Their ATLAS light curves resemble SNe (possibly faint or highly reddened) but the classification spectra are dominated by host galaxy light. AT 2020wia has an SN-like light curve and is coincident with the core of the galaxy 2MASS J05485394+1911311, which has no catalogued redshift. A spectrum obtained by ePESSTO+ showed a red continuum and strong galaxy emission lines at $z = 0.021$, but a definitive classification was not possible to determine from the spectrum (N. Ihanec et al. 2020). AT 2021aks has a light curve that is also SN-like (albeit incomplete, with the early rise missing) and its spectrum was also dominated by galaxy light (J. Terwel et al. 2021). We reassigned these two transients as unclassified since their spectral type is unclear.

AT 2023dm is an interesting nuclear transient and also in the Galactic plane ($b = 3.23^\circ$) with a broad light curve ($\tau_{1/2} \sim 50$ d). It has a constant colour and is coincident with the core of a nucleated galaxy, both of which may indicate a TDE. The ePESSTO+ classification spectrum shows narrow He I, He II, and

N III emission lines, possibly due to Bowen fluorescence at $z = 0.021$. This event was classified as 'Other' on the TNS (T. Moore et al. 2023a). It is not clear if this is nuclear activity in an AGN, but it has been at a consistently elevated level after the flare, which may also indicate a TDE plateau (A. Mummery et al. 2024). This object is worth investigating further, but we refrain from classifying it as a TDE here, instead assigning it as 'AGN' (Table 3).

3.2 Host galaxy separation

Figs 8 and 9 show cumulative frequency diagrams of projected host galaxy separations for the key spectral types in the sample. We show them in both angular separation (arcsec) and in units of kiloparsec (kpc), assuming a distance from the host redshift. The histogram shows that the two CCSN families of SESNe and SNe II show a similar distribution for host galaxy separation, with all CCSNe occurring within ∼30 kpc. Based on a literature sample of 177 CCSNe, J. P. Anderson & P. A. James (2009) reported a strong deficit (excess) of SNe II (SESNe) in the central regions of their host galaxies. We do not recover this trend within the ATLAS100 sample, which consists of 688 SNe II and 240 SESNe (total of 928 CCSNe). The J. P. Anderson & P. A. James (2009) sample was based on publicly announced SN discoveries from many different surveys, with differing sensitivities, and many were not difference image based. The larger ATLAS100 sample and uniform data and analysis methods does not recover a significant difference, although in each bin (up to a projected separation of 12 kpc), the SESNe have a slightly higher frequency of occurrence. The SESN sample has a 90-percentile separation of 8 kpc, compared to 10 kpc for SNe II. A two-sample Kolmogorov–Smirnov (KS) test performed on the host galaxy separations for SESNe and SNe II yields a p-value of 0.4, suggesting there is no evidence these are drawn from different underlying populations.

Like the CCSNe in the sample, the bulk of SNe Ia (∼90 per cent) occur within a projected separation of 12 kpc. A small but measurable fraction of SNe Ia show an extended distribution; this is due to sub-classes such as Ia-91bg showing a preference for remote locations in early-type galaxies (e.g. G. Dimitriadis et al. 2025). There are 12 SNe Ia (2.2 per cent) that show projected separations of $R_{\rm proj} > 30$ kpc in our sample, 5 of which are classified as Ia-91bg. The distribution for unclassified events shows a more extended tail compared to CCSNe, but less so than SNe Ia. As suggested previously based on Fig. 5, the majority of the unclassified sub-sample seems to be a combination of CCSNe and SNe Ia, rather than representing faint and/or unusual subclasses of transients. This further supports our assertion that the unclassified sample is not inherently different in nature to the classified sample, and does not introduce a strong and obvious bias into the relative rates.

Fig. 10 shows a similar cumulative frequency histogram of projected radial separation (kpc) for gap transients in the sample – 12 LRNe, 11 ILRTs, 8 CaSTs, and 3 LBVs. LBVs, ILRTs, and LRNe are confined to within ∼12 kpc from their host galaxies. CaSTs on the other hand show a remarkably extended radial distribution. This is consistent with the already recognized tendency for these to occur in remote locations around early-type hosts (R. J. Foley 2015), but our volume-limited sample demonstrates this quantitatively.

3.3 Light curve fitting

For all transients in the ATLAS100 sample, ATLAS photometry was binned and cleaned as described in Section 2.5. We fit the ATLAS light curves of all transients in the sample with a suitable model, discussed in more detail below, to estimate peak magnitudes and a characteristic time-scale or duration for the light curve, defined as the time above half peak flux (D. A. Perley et al. 2020). In general, SNe Ia and Ib/c events show simpler light curves with a typical rise and fall, whereas SNe II tend to be longer lived with a more complex light curve morphology. The observing strategy of ATLAS is such that the c band is only used around dark time. Most of the light curve data are thus obtained in the o-band and so we restrict light curve fitting to this band.

We impose additional quality cuts in the light curve fitting routine. We require ≥2 ATLAS non-detections in the time window between the TNS discovery epoch and 15 d prior. This condition ensures reasonable pre-explosion constraints and also eliminates transients emerging from solar conjunction and thus lacking a light curve peak and pre-discovery non-detections. Additionally, we require ≥2 measurements during the rising phase of the light curve, ≥10 points within TNS discovery epoch and 90 d after, and a peak observed flux, $f \geq 150$ μJy (corresponding to a peak observed magnitude of ∼18.5 AB mag). Since the limiting magnitude of ATLAS is ∼19.5, the latter ensures sufficient signal-to-noise (S/N) around peak for a robust light curve fit. These strict quality cuts removed 942 transients. A further 51 transients were rejected, either due to low S/N data, lack of photometric coverage around peak, or complex light curve morphology that was not fully captured by the simple analytical models. Our final sample consists of 736 transients that passed our quality cuts (Table 3).The light curve fitting procedure for different SN types is described in more detail in the following sections.

3.3.1 SESNe

We fit the light curves of SNe Ibc and SNe IIb in the sample that passed the quality cuts with the Bazin model (G. Bazin et al. 2009), an analytic model with an exponential rise and fall, defined as

$$f(t) = A\frac{e^{-(t-t_0)/\tau_{\rm fall}}}{1+e^{(t-t_0)/\tau_{\rm rise}}} + B. \quad (1)$$

In general, with the exception of double-peaked light curves (e.g. shock-cooling tails in SNe IIb) or other peculiarities (such as precursor emission), we find the Bazin model provides an adequate fit to most SESN light curves. For SNe IIb, the early shock-cooling component (if present) was excluded from the light curve fit. The model has five free parameters (A, B, t_0, $\tau_{\rm rise}$, and $\tau_{\rm fall}$), and the fit was implemented using LMFIT (M. Newville et al. 2025). The model constructed from the best-fitting parameters was used to derive the peak flux and the light curve duration; i.e. the time above half peak flux.

3.3.2 SNe Ia

The SNe Ia that passed our quality cuts were also fit with the Bazin model described above. Although the Bazin model generally provides a reasonable fit for the rising light curves of SNe Ia, the post-peak light curve fit was found to be poor. Most SNe Ia show a pronounced secondary maximum or 'shoulder' occurring roughly 3 weeks past the primary maximum (D. Kasen 2006),

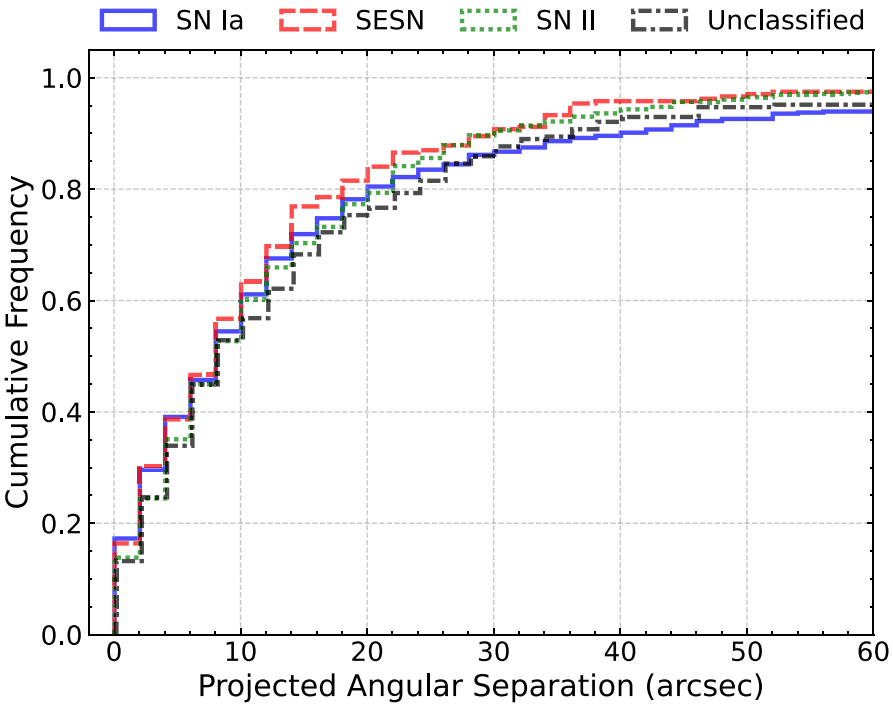

Figure 8. Projected angular separation (arcsec) from the host galaxy for the key distinct spectroscopic types in the sample: SNe Ia, SNe II, SESNe, and unclassified transients.

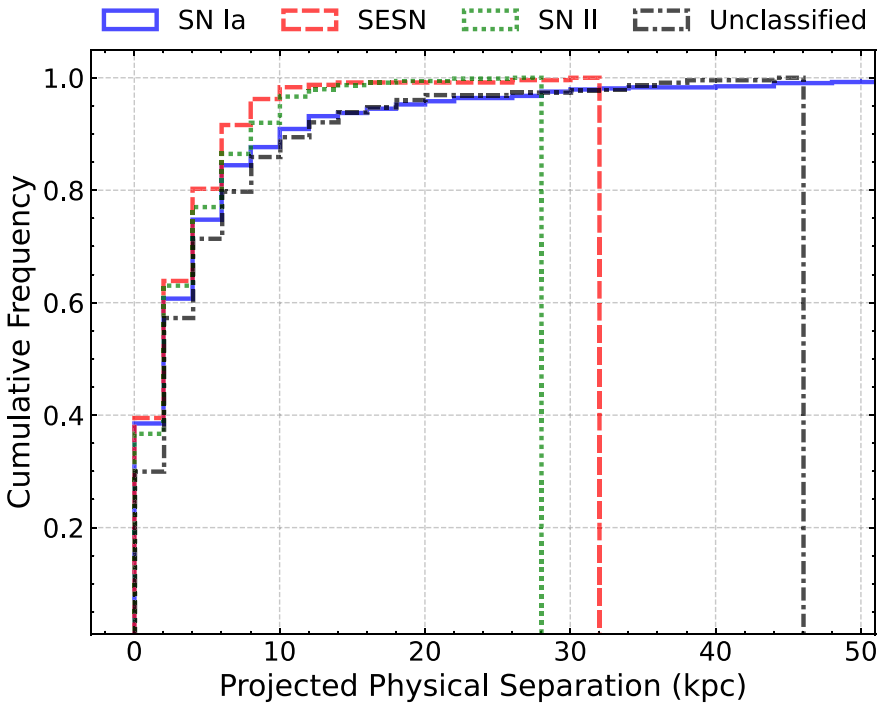

Figure 9. Projected physical separation (in kiloparsec) from the host galaxy for the key distinct spectroscopic types in the sample, including SNe Ia, SNe II, SESNe, and unclassified events.

particularly conspicuous in the near-infrared (NIR) but also noticeable in the redder optical bands. It is visible in well-sampled ATLAS light curves in the *o* band. This feature is understandably not captured in the Bazin model and it affects the measurement of the light curve duration. Thus for SNe Ia, we instead use the SALT2 model (J. Guy et al. 2007) implemented in the SNCOSMO package (K. Barbary et al. 2025). We note that the secondary maximum is weak or absent in certain sub-classes of SNe Ia such as Ia-91bg, Iax, Ia-02es, and Ia-03fg. For Ia-91bg, we use the *nugent-sn91bg* model (P. Nugent, A. Kim & S. Perlmutter 2002) in SNCOSMO. The Bazin model produces a better fit for the other peculiar sub-classes Iax, Ia-02es, and Ia-03fg, and we thus use

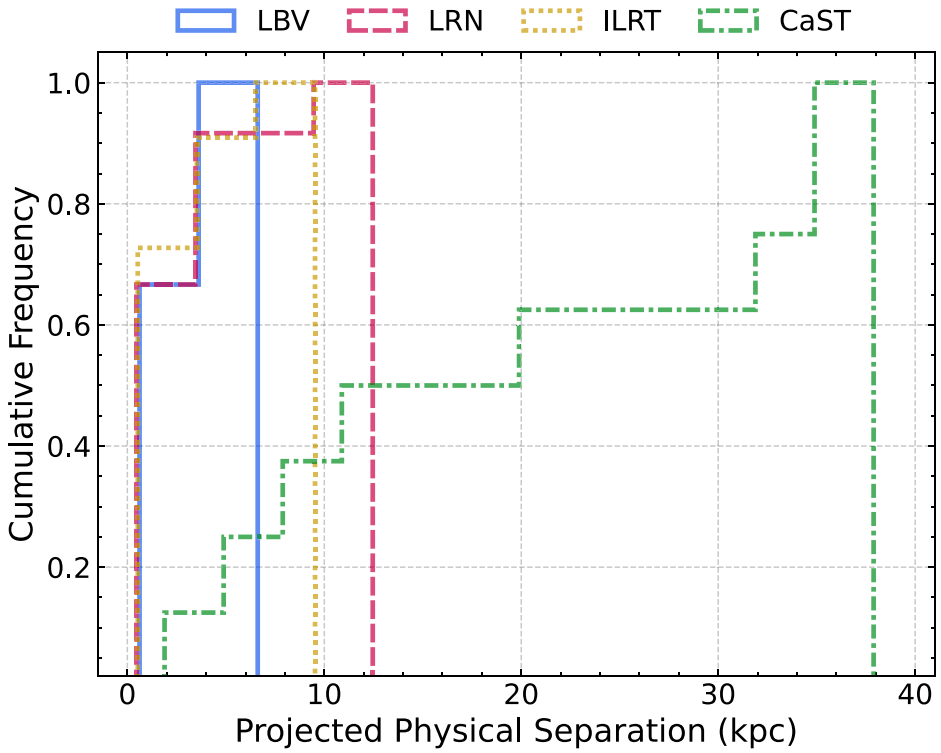

Figure 10. Projected physical separation (in kiloparsec) from the host galaxy for gap transient families in the sample including LBVs, LRNe, ILRTs, and CaSTs.

the derived peak fluxes and durations for these from the Bazin fit.

3.3.3 SNe II

The SN II light curves were fit with the analytical model presented by V. A. Villar et al. (2019). This model is similar to the Bazin with two additional free parameters for the plateau component often seen in SN II light curves. SNe II are a diverse family of transients with a rich variety in light curve morphology, and in some cases this simple model is unable to capture light curve features, in which case the estimated peak and light curve duration is unreliable. The fits were inspected visually and discarded if the overall light curve shape and/or peak was poorly fit.

3.3.4 Unclassified and other transients

For unclassified transients, and transients belonging to the 'Other' category (Fig. 7), we use the Bazin model to fit the light curves. The Bazin model overall does reasonably for unclassified SNe, although some are likely SNe II. The Bazin model also produces reasonable fits for ILRTs, CaSTs, and TDEs. In case the light curve fits were found to be inadequate, and if the light curve coverage/cadence was good, the duration ($\tau_{1/2}$) was estimated simply from the observed light curve.

3.4 Duration–luminosity relations and science highlights

The peak fluxes derived from the model fits were corrected for foreground MW extinction. For each transient, we also derive a peak observed flux and observed duration, measured directly from the binned, cleaned ATLAS light curve. For well-sampled light curves, the observed values show a good match with the model-derived parameters. However, when there are gaps in the light curve coverage, the directly measured values are unreliable and generally underestimate the light curve duration and/or the peak flux. Fig. 11 shows ATLAS *o*-band light curves for selected events belonging to different spectroscopic types, along with the best-fitting model. The shaded region represents the time above half the peak flux derived from the model. Table 3 summarizes the different spectroscopic sub-classes in ATLAS100 and their median durations and peak luminosities derived from the light curve fitting.

A duration–luminosity diagram is a succinct way to visualize and compare different transient sub-classes (S. R. Kulkarni et al. 2007; M. M. Kasliwal 2012; V. A. Villar et al. 2017). Fig. 12 represents the ATLAS100 sample in this phase space, where the characteristic time-scale or duration of the light curve and peak luminosity were estimated using the methodology described in Section 3.3. For context, the rapidly evolving kilonova AT 2017gfo (e.g. E. Pian et al. 2017; S. J. Smartt et al. 2017) was added to the plot, along with other fast transients such as AT 2018cow (S. J. Prentice et al. 2018; D. A. Perley et al. 2019) and AT 2018kzr (O. R. McBrien et al. 2019; J. H. Gillanders, S. A. Sim & S. J. Smartt 2020). For AT 2017gfo, the light curve duration and *o*-band peak luminosity was estimated using a synthetic *o*-band light curve model generated following M. Nicholl et al. (2021). AT 2018cow is part of the ATLAS100 sample but did not pass the light curve quality cuts due to the rapid evolution. For AT 2018cow and AT 2018kzr, we use the duration and luminosity estimates provided by D. A. Perley et al. (2020).

The ATLAS100 sample represents the most nearby and therefore most well-studied SNe, and there are several publications in the literature presenting detailed studies of individual events

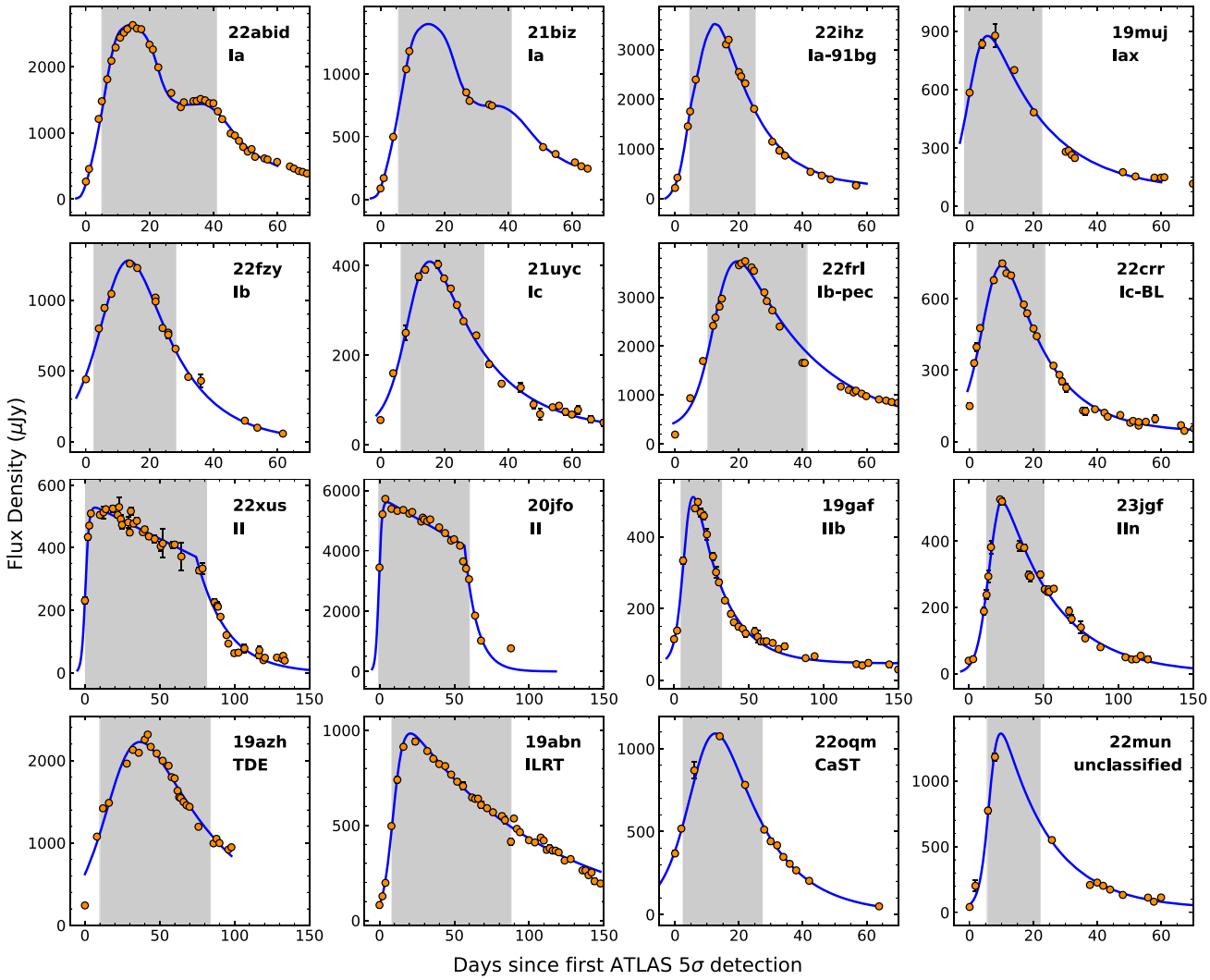

Figure 11. Sample ATLAS *o*-band light curves of ATLAS100 transients across different spectral types and varying light curve quality and coverage. Also shown for each light curve is the best-fitting model that was used to derive the peak flux and the characteristic time-scale or duration of the light curve. The shaded region represents the measured duration above half the peak flux.

in the sample. ATLAS photometry has contributed extensively to several of these studies. Here, we present a brief and non-exhaustive overview of the variety of transients in the ATLAS100 sample.

3.4.1 Hydrogen-rich SNe

SNe II comprise the most abundant spectroscopic class within the ATLAS100 sample (Fig. 6). For the duration–luminosity diagram, we further sub-divide SNe II into II-norm, IIn, II-pec, and IIb (SNe IIb are discussed further in Section 3.4.2). From the duration–luminosity diagram (Fig. 12), it is clear that SNe II-norm tend to have longer time-scales, albeit with a large variation in both time-scale and peak luminosity. The median time-scale for II-norm that passed the light curve quality cuts (251 out of the total 643) is 81.5 (27.6) d, where the standard deviation is indicated in the parentheses. The median peak absolute magnitude for SNe II-norm in the *o* band is −17.0 (0.7) mag AB. SNe IIn on the other hand show a slightly lower median time-scale of 65.7 (26.3) d, with a generally higher peak luminosity of −17.9 (0.9).

The sample includes SN 2023ixf, one of the nearest and most well-studied SNe II in the last decade, with evidence of complex, asymmetric circumstellar material or CSM (e.g. K. A. Bostroem et al. 2023; W. V. Jacobson-Galán et al. 2023). The variable, red supergiant (RSG) progenitor of SN 2023ixf likely suffered multiple eruptive mass-loss episodes shortly before explosion (D. Hiramatsu et al. 2023; J. E. Jencson et al. 2023; C. D. Kilpatrick et al. 2023). Another nearby type II SN 2024ggi at ∼7 Mpc was discovered by ATLAS within hours of explosion (S. Srivastav et al. 2024; T.-W. Chen et al. 2025), also showing evidence of CSM interaction (M. Shrestha et al. 2024) and a RSG progenitor identified in archival *Hubble Space Telescope* (*HST*) and *Spitzer* data (D. Xiang et al. 2024). SN 2024ggi is not part of the current sample but will be included in a future extension of the catalogue. The sample includes short plateau events such as SN 2018gj (R. S. Teja et al. 2023) and SN 2020jfo (J. Sollerman et al. 2021), and low luminosity events like SN 2018hwm (A. Reguitti et al. 2021), SN 2018is (R. Dastidar et al. 2025), SN 2018lab (J. Pearson et al. 2023), SN 2020cxd (S. Yang et al. 2021; A. Kozyreva et al. 2022), and SN 2021aai (G. Valerin et al. 2022). A sample study of 330

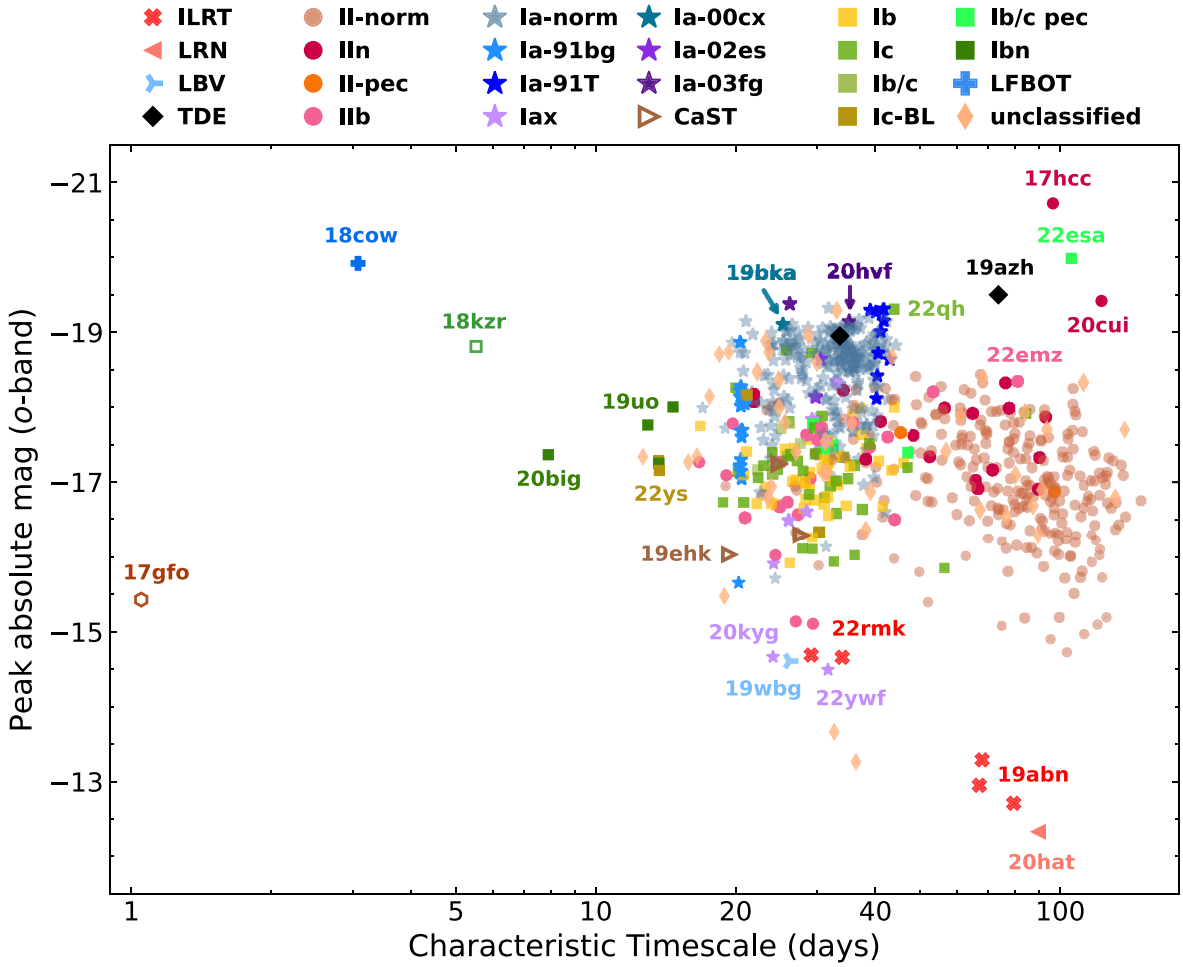

Figure 12. Peak luminosity versus rest-frame time-scale or duration in *o* band for all transients in the ATLAS100 sample that passed the light curve quality cuts. A selection of individual events across different spectral types are highlighted in the plot. The rapidly evolving transients AT 2017gfo and AT 2018kzr are not part of the sample but are shown for context.

nearby SNe IIP within 200 Mpc in ZTF found 16 low luminosity ($M_r \geq -16$) events (K. K. Das et al. 2025a), likely originating from low mass RSG progenitors. SN 2020tlf represents the first case of a precursor detected in a normal SN IIP/L (W. V. Jacobson-Galán et al. 2022a), starting months prior to explosion.

Interacting SNe IIn often show precursor outbursts months to years preceding terminal explosion (E. O. Ofek et al. 2014; N. Smith 2016), with ∼26 per cent of ZTF SNe IIn showing a precursor brighter than −13 within 3 months of explosion (N. L. Strotjohann et al. 2021). Several SNe IIn in the ATLAS100 sample show precursor outbursts detected in pre-explosion imagery – these include SN 2018cnf (A. Pastorello et al. 2019b), SN 2020pvb (N. Elias-Rosa et al. 2024), and SN 2023ldh (A. Pastorello et al. 2025). Owing to its sensitivity and long baseline, Pan-STARRS (K. C. Chambers et al. 2016) is well-suited for detection of faint precursors as shown in the search for faint transients in the Pan-STARRS surveys by M. D. Fulton et al. (2025).

A forthcoming study will focus on the sub-sample of SNe IIn within 100 Mpc with ATLAS, combined with archival Pan-STARRS photometry to look for precursor outbursts. We note here that out of the 41 SNe IIn in this sample with declination $\delta > -40$ °, seven events (17 per cent) have precursors in Pan-STARRS. This fraction is not corrected for survey sensitivity, cadence, sky coverage etc. and therefore represents a lower limit; the true fraction is presumably higher (A. Reguitti et al. 2024).

3.4.2 *Stripped Envelope SNe*

The progenitors of SESNe (IIb, Ib, and Ic) have been proposed to be more massive main-sequence stars than their H-rich CCSN counterparts (L. Dessart et al. 2011), although mass transfer in close binary systems likely plays a significant role in stripping the envelope (P. Podsiadlowski, P. C. Joss & J. J. L. Hsu 1992; N. Smith 2014; S.-C. Yoon, L. Dessart & A. Clocchiatti 2017). Explosion parameters and ejecta masses estimated for large samples of SESNe are generally not as extreme as one would expect if single, massive Wolf–Rayet (WR) progenitors were the dominant channel, favouring a binary progenitor for most SESNe (e.g. Z. Cano 2013; J. D. Lyman et al. 2016; F. Taddia et al. 2018; S. J. Prentice et al. 2019).

SNe Ib and Ic in the ATLAS100 sample occupy broadly similar regions in the duration–luminosity diagram, with median peak absolute magnitudes of −17.1 (0.4) and −17.2 (0.8), and median time-scales of 30.9 (6.2) and 29.3 (11.6) d for Ib and Ic, respectively. SNe IIb show similar median peak luminosity of −17.3 (0.8) and time-scale of 28.7 (13.7) d, but with a larger scat-

ter in their light curve duration. In our sample, SNe Ic-BL appear to have a shorter median duration than both the narrower lined Ib, Ic, and Ib/c events. While we have only four objects that meet the $N_{\rm cut}$ criterion, they do not appear significantly brighter or broader than the rest of the Ibc sample (see Table 3), with a median duration of 17.4 (6.8) d, in contrast to ∼30 d duration for the rest of the SESN population. This is also seen in the sample of S. J. Prentice et al. (2019) at lower statistical significance. It is perhaps surprising that SNe Ic-BL show shorter durations compared to the rest of the SESN population, but previous work has combined inhomogeneous samples of SNe Ic-BL over large redshift ranges. We defer a quantitative analysis of the ejecta and ^{56}Ni masses to a future paper, in order to constrain powering mechanisms (as in Ó. Rodríguez, E. Nakar & D. Maoz 2024).

The sample includes the extraordinary Ic SN 2022jli that exhibited a ∼12.5 d periodicity in its light curve (T. Moore et al. 2023b; R. Cartier et al. 2024; P. Chen et al. 2024), likely originating from the newly formed compact object (neutron star or black hole) interacting with its binary companion. The unusual and luminous Ic event SN 2022esa exhibits a similar periodicity of ∼32 d with multiple cycles over 200 d (K. Maeda et al. 2026). SN 2022esa is classified on the TNS as SN Ia-CSM; we reclassify it as SN Ic-pec in our sample. SN 2023aew was another enigmatic transient with a double-peaked light curve, transforming from a SN IIb during the initial peak to a SN Ib/c during the second peak (T. Kangas et al. 2024; Y. Sharma et al. 2024). The Ic-BL SN 2022xxf also showed a double-peaked light curve (H. Kuncarayakti et al. 2023), where the second peak was interpreted as CSM interaction with H/He-poor material, likely expelled from the progenitor shortly before explosion. The Ib SNe 2019oys and 2019yvr showed evidence of interaction with H-rich CSM at late times (J. Sollerman et al. 2020; L. Ferrari et al. 2024), whereas the interacting Ibn SN 2023fyq displayed precursor activity from months prior to explosion (S. J. Brennan et al. 2024; Y. Dong et al. 2024). The sample also includes the Ibn SN 2019uo (A. Gangopadhyay et al. 2020) and the Icn SN 2019jc (C. Pellegrino et al. 2022b).

A rare and rather elusive sub-population of long-duration SESNe was recently reported by E. Karamehmetoglu et al. (2023) in PTF survey data, accounting for ∼6 per cent of the SESN rate. These long-duration SESNe show a preference for low-metallicity, star-forming hosts, favouring massive progenitors with much higher ejecta masses compared to normal Ib/c events (E. Karamehmetoglu et al. 2023). Additionally, S. Gomez et al. (2022) studied a population of luminous SNe or LSNe with $-19 > M_r^{\rm peak} > -20$. These events form a link between normal SNe Ib/c and SLSN-I populations in terms of their durations and peak luminosities, and could be powered by an additional energy source such as magnetar spin-down along with radioactive ^{56}Ni (S. Gomez et al. 2022).

We identify a handful of SESNe in the duration–luminosity diagram with unusually long time-scales of $\gtrsim$ 40 d. These include the luminous Ic SN 2022qh with $M_o^{\rm peak} \approx -19.3$, and the surprisingly long-lived Ic SN 2020sgf and IIb SN 2022emz with time-scales of $\gtrsim$ 80 d. A detailed investigation of SESNe in ATLAS, with particular emphasis on these long-rising and long-duration SESNe will be presented in a forthcoming paper.

3.4.3 *Thermonuclear SNe*

SNe Ia-norm form a reasonably tight cluster in the duration–luminosity diagram, although there are a few highly extinguished events due to host reddening at the low luminosity end. The median peak absolute magnitude of −18.7 (0.6) and median time-scale of 33.4 (5.6) d reflects the relative homogeneity as expected. The Ia-91T and Ia-91bg sub-classes have median peak absolute magnitudes of −19.0 (0.4) and −17.7 (0.7), with median time-scales of 40.5 (1.1) and 20.6 (0.2) d, respectively. SNe Iax are the most diverse sub-class with a median absolute magnitude of −16.6 (1.3). Despite their relative homogeneity, a rich diversity within thermonuclear SNe is undeniably present (S. Taubenberger 2017), hinting at multiple progenitors and/or explosion mechanisms.

We highlight the interesting event SN 2019bka classified as Ia-91T on the TNS (S. Schuldt et al. 2019). Although the classification spectrum does resemble Ia-91T, we measure a duration of only ∼ 24 d, significantly faster evolving than the rest of the Ia-91T sub-population in the sample (with median duration of 40.5 ± 1.1 d). SN 2019bka thus stands out in the duration–luminosity diagram as an outlier among Ia-91T events. The transient is in a remote location, with a projected separation of 41 kpc from the elliptical galaxy CGCG 097–109. Given these properties, SN 2019bka possibly belongs to the rare sub-class of peculiar 00cx-like SNe Ia (J. M. Silverman et al. 2013).

The faintest SNe Iax in the sample are SN 2019gsc ($M_r^{\rm peak} \approx -14.0$; L. Tomasella et al. 2020; S. Srivastav et al. 2020a), SN 2022ywf ($M_o^{\rm peak} \approx -14.5$), and SN 2020kyg ($M_o^{\rm peak} \approx -14.7$; S. Srivastav et al. 2022). SN 2019muj ($M_r^{\rm peak} \approx -16.4$; B. Barna et al. 2021) and SN 2019ovu ($M_o^{\rm peak} \approx -16.5$) are intermediate luminosity Iax events, whereas SN 2020sck ($M_o^{\rm peak} \approx -17.8$; A. Dutta et al. 2022) and SN 2020udy ($M_o^{\rm peak} \approx -18.3$; K. Maguire et al. 2023; M. Singh et al. 2024) represent the luminous end of the distribution. The faint Iax events SN 2019ttf ($M_r \approx -13.7$, although with likely significant host extinction), SN 2021fcg ($M_r^{\rm peak} \lesssim -13$; V. R. Karambelkar et al. 2021), and SN 2023bsr ($M_o^{\rm peak} \approx -13.5$) were discovered during the time window of this sample, but were not registered to TNS since they did not generate at least three 5σ detections in ATLAS on any single epoch, although forced photometry does reveal lower significance (3σ) detections around peak for all three events.

The sample includes well-studied Ia-norm events with an early excess in their light curves such as SN 2018oh (G. Dimitriadis et al. 2019; W. Li et al. 2019; B. J. Shappee et al. 2019), SN 2019np (H. Sai et al. 2022), SN 2021hpr (G. Lim et al. 2023), and SN 2023bee (G. Hosseinzadeh et al. 2023; Q. Wang et al. 2024). This feature has been attributed to different powering mechanisms such as ejecta–companion interaction (D. Kasen 2010), ejecta–CSM interaction (A. L. Piro & V. S. Morozova 2016), surface ^{56}Ni distribution (M. R. Magee & K. Maguire 2020), and helium shell detonation (A. Polin, P. Nugent & D. Kasen 2019). We note however that the term 'early excess' is quite broad and not straightforward to quantify, since it depends on the cadence and quality of the observed data and the model/method used to fit the early light curve. The morphology of the early excess features reported in the aforementioned Ia-norm events is markedly distinct from the prominent spike-like, non-monotonic early excess features (J.-a. Jiang et al. 2018; W. B. Hoogendam et al. 2024) seen in recent Ia-02es and Ia-03fg events like iPTF14atg (Y. Cao et al. 2015), SN 2019yvq (A. A. Miller et al. 2020; J. Burke et al. 2021), SN 2020hvf (J.-a. Jiang et al. 2021), SN 2021zny (G. Dimitriadis et al. 2023), SN 2022ilv (S. Srivastav et al. 2023a), SN 2022vqz (G. Xi et al. 2024), SN 2022ywc (S. Srivastav et al. 2023b), SN 2022abom (M. D. Fulton et al. 2025), and SN 2021qvo (I. A. A. Paniagua et al. 2026). Among these events, SNe 2019yvq, 2020hvf, and 2022vqz are part of the

ATLAS100 sample. Interaction with $\sim 10^{-3}$–10^{-1} $M_\odot$ of CSM placed $\sim 10^{13}$–10^{15} cm from the WD progenitor is a promising mechanism to explain the duration, colour, and luminosity of these observed early excess features (e.g. A. L. Piro & V. S. Morozova 2016; T. J. Moriya et al. 2023). The CSM itself could plausibly arise as a natural outcome of mass loss in a double-degenerate system as tidally stripped material from the secondary WD (C. Raskin & D. Kasen 2013; M. Dan et al. 2014), or from wind-driven material launched in polar directions from the accretion disc formed following the disruption of the secondary WD (disk-originated matter; N. Levanon & N. Soker 2017). Nebular spectra of some members belonging to both Ia-02es and Ia-03fg subclasses have shown narrow [O I] emission (S. Taubenberger et al. 2013, 2019; M. Kromer et al. 2016; G. Dimitriadis et al. 2023; M. R. Siebert et al. 2024), considered to be a signature of a violent WD merger (R. Pakmor et al. 2012; M. Kromer et al. 2013). Moreover, mid-infrared spectra from *JWST* revealed strong [Ne II] emission at 12.81 μm in the nebular spectra of the Ia-03fg SN 2022pul (L. A. Kwok et al. 2024), a feature that is only predicted by models involving a violent merger (S. Blondin et al. 2023). This highlights the diagnostic power of combining early-time and late-time observations, both of which favour a WD merger scenario for these peculiar SN Ia subtypes. A sample of recent Ia-02es and Ia-03fg events displaying early excess features in combined ATLAS, ZTF, and Pan-STARRS data will be presented in a forthcoming paper.

Beyond their utility for in-depth studies of individual objects and sub-populations, low-redshift SNe Ia play a critical role in anchoring the Hubble diagram for cosmological analyses (R. J. Foley et al. 2018; M. Vincenzi et al. 2025). With the advent of next-generation surveys like the Legacy Survey of Space and Time (LSST; Ž. Ivezić et al. 2019), which will observe unprecedented numbers of high-redshift SNe Ia, the precision of cosmological constraints will increasingly rely on the quality and completeness of the low-z anchor sample. A well-characterized nearby SN Ia population with uniform selection and well-understood systematics is essential to control calibration uncertainties and standardization biases that propagate through to measurements of dark energy parameters. The ATLAS survey, with its high cadence, wide field of view and all-sky coverage, and 10-yr catalogue, is not only well-suited to providing a cosmologically useful low-z SN Ia sample, but is actively being used to prepare such a sample. A coordinated series of forthcoming papers will present the first data release of the cosmological ATLAS SN Ia sample, including details of photometric calibration (E. G. Marlin et al. 2025), light curve cleaning and fitting, and survey simulations.

3.4.4 Other transients

A small fraction (2.3 per cent) of transients in ATLAS100 is classified as 'Other' as discussed in Section 3.1.2 (Figs 6 and 7). The Other category encompasses an eclectic and interesting mix of transient classes including LFBOTS, TDEs, LBVs, LRNe, ILRTs, and CaSTs.

The ATLAS100 sample includes four known and well-studied TDEs – AT 2019azh (e.g. X.-L. Liu et al. 2022), AT 2019qiz (e.g. M. Nicholl et al. 2020; T. Hung et al. 2021), AT 2021ehb (Y. Yao et al. 2022), and AT 2022dsb (A. Malyali et al. 2024).

The sample includes well-studied LRNe like AT 2017jfs (A. Pastorello et al. 2019a), AT 2018bwo (N. Blagorodnova et al. 2021), AT 2020hat and AT 2020kog (A. Pastorello et al. 2021), AT 2021afy and AT 2021blu (A. Pastorello et al. 2023), and AT 2021biy (Y. Z. Cai et al. 2022). A massive progenitor candidate of ~ 50 $M_\odot$ was identified in archival data for the luminous LRN AT 2021aess (Guidolin et al. submitted), also part of the sample. The volumetric rate of LRNe is a strong function of luminosity (V. R. Karambelkar et al. 2023), with luminous LRNe such as AT 2021aess being intrinsically rare. LRNe are generally considered to be the outcome of non-terminal events associated either with common envelope ejections or stellar mergers in close binary systems (N. Ivanova et al. 2013; N. Blagorodnova et al. 2017). ILRTs on the other hand may be terminal electron capture SNe (ECSNe) from super-AGB progenitors (M. T. Botticella et al. 2009). ILRTs in the sample include AT 2018aes (Y. Z. Cai et al. 2021), AT 2019abn, AT 2019ahd and AT 2019udc (G. Valerin et al. 2025a, b), and AT 2022fnm (S. Moran et al. 2024).

LBVs comprise another diverse sub-class of gap transients associated with non-terminal eruptions in evolved, massive stellar systems (N. Smith et al. 2011b). Also referred to sometimes as 'SN-impostors', LBV/impostor events have been observed as precursors of interacting SNe in a handful of cases (e.g. A. Pastorello et al. 2007; M. Fraser et al. 2013). Owing to their intermediate luminosity and erratic, often rapid decline rates, luminous LBV eruptions occupy a region overlapping with kilonovae in the duration–luminosity diagram and were identified as major contaminants in the search for kilonovae in Pan-STARRS survey data (O. R. McBrien et al. 2021; M. D. Fulton et al. 2025). Their bluer colours and longer survey baselines (capturing multiple eruptions) can be used to distinguish them from kilonovae.

CaSTs constitute a family of low-luminosity transients with poorly understood progenitors, with recent evidence for distinct sub-populations (Ca-Ia and Ca-Ib/c; K. De et al. 2020), indicating multiple underlying progenitor channels could be responsible. These include core-collapse in highly stripped stars (D. Milisavljevic et al. 2017) and weak explosions involving low-mass WD progenitors (R. Lunnan et al. 2017). A significant fraction of CaSTs occur at large projected separations from early-type host galaxies (J. D. Lyman et al. 2014). The host environments for this Ca–Ia sub-population show no evidence of current star formation and favour old stellar populations, interpreted as evidence for WD progenitors. Interestingly, a number of recent, nearby CaSTs discovered young show double-peaked light curves – these include SN 2019ehk (W. V. Jacobson-Galán et al. 2020), SN 2021gno (K. Ertini et al. 2023), SN 2021inl (W. V. Jacobson-Galán et al. 2022b), and SN 2022oqm (I. Irani et al. 2024; S. K. Yadavalli et al. 2024), all part of the ATLAS100 sample. The primary peak (or early excess) in SN 2021gno and SN 2021inl that lasts for a few days was modelled using interaction with confined CSM (W. V. Jacobson-Galán et al. 2022b), who inferred a CSM mass of $\lesssim 10^{-2}$ $M_\odot$ and a radial extent of $\sim 10^{13}$–10^{14} cm. Moreover, luminous and rapidly decaying X-ray emission within a day of explosion has been detected for two CaSTs, SN 2019ehk (W. V. Jacobson-Galán et al. 2020) and SN 2021gno (W. V. Jacobson-Galán et al. 2022b), consistent with the CSM parameters derived from modelling the multicolour light curve during the early excess (W. V. Jacobson-Galán et al. 2022b). We note that these CSM parameters are similar to those inferred from modelling the early excess features observed in recent Ia-02es and Ia-03fg events (Section 3.4.3), suggesting WD mergers may be the unifying link across a range of peculiar thermonuclear SN sub-classes spanning faint CaSTs, to sub-luminous Ia-02es and overluminous Ia-03fg events. Variations in primary WD mass, binary mass ratio, WD compositions, and the inherently asymmetric nature of WD mergers

could potentially provide a natural explanation for the diversity in observed properties across these sub-types. Recent simulations of low-mass WD mergers, involving either a hybrid HeCO WD disrupting a CO WD (Y. Zenati et al. 2023), or a CO WD merging with a He WD (J. Morán-Fraile et al. 2024; F. P. Callan et al. 2025) predict weak/faint thermonuclear explosions and thus present a promising avenue for further investigation.

3.5 Sample purity and completeness

In this section, we attempt to quantify the purity and completeness of the ATLAS100 sample.

3.5.1 Redshift completeness of galaxy catalogues and implications for completeness

We have used a combination of host galaxy redshifts and redshifts derived from the transient (or its host) during follow-up. Here, we consider our completeness due to both of these selection effects.

The redshift completeness fraction, or RCF, is defined as the fraction of SN host galaxies with known spectroscopic redshift information (prior to the discovery of the transient) relative to the total number of transients in the sample. Every transient in the sample has a securely identified host galaxy detected in optical imaging. We find no case of a transient which has a redshift within the $z \leq 0.025$ limit that has either no detection of a nearby host or is separated by a large spatial extent ($R_{\rm proj} \geq 50$ kpc) and has a discrepant redshift. Essentially, almost every transient is associated with a unique host that can be optically identified. In a handful of rare cases (SN 2019be, SN 2019bkc, and SN 2020ags), the location of the transient is within a cluster of galaxies where a unique host association is not obvious. However, the redshift of the transient inferred from the classification spectrum is consistent with the spectroscopic redshift of the potential hosts, and is thus secure. Therefore the RCF is a measure of the redshift completeness down to a galaxy brightness, or mass, limit. The RCF is expected to be fairly high in the local volume, falling off steeply as a function of distance and host galaxy luminosity (C. Fremling et al. 2020). S. R. Kulkarni et al. (2018) estimated an RCF of ∼80 per cent for $z \leq 0.03$, corresponding to a distance of ∼130 Mpc. The ATLAS100 sample has an RCF of 83 per cent; i.e. prior host galaxy redshifts were not available for 17 per cent of the spectroscopically classified transients in the sample. This is consistent with previous expectations for RCF in the local volume (S. R. Kulkarni et al. 2018; C. Fremling et al. 2020). For this 17 per cent, the redshifts come mostly from the broad lines of the SN; e.g. from the redshift derived through the cross-correlation of the spectrum in SNID. We examine the distribution of host galaxy magnitudes with and without a prior catalogued redshift in Fig. 13. It is clear that the hosts identified by SHERLOCK without a catalogued redshift represent a fainter population, as expected. Finally, we examine the redshift completeness of the NED Local Volume Sample (NED-LVS; D. O. Cook et al. 2023) and LASr (D. Asmus et al. 2020) catalogues, the two major sources for a host galaxy spectroscopic redshift for SHERLOCK within 100 Mpc (Fig. 2). NED-LVS is a sub-set of NED consisting of ∼2 million galaxies within 1000 Mpc. We cleaned the NED-LVS catalogue by removing photometric redshifts, and any redshifts marked with an 'unreliable' qualifier. Fig. 14 shows the redshift distribution of galaxies in the NED-LVS and LASr catalogues within $z \leq 0.03$. The dashed line representing volume is scaled to the redshift bin at $z = 0.01$, since at low redshift the distribution of galaxies is governed by the Local Group and Virgo Supercluster.

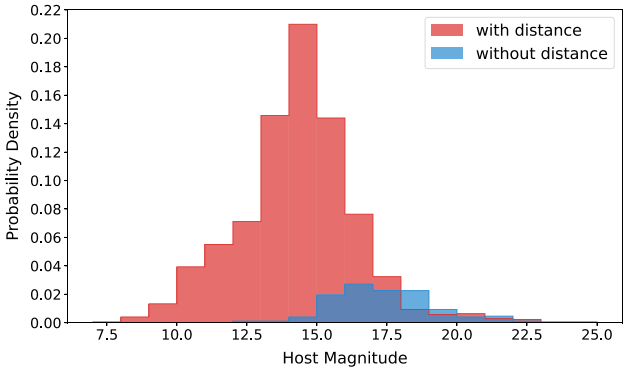

Figure 13. Histogram showing the brightness distribution of host galaxies in ATLAS100 from SHERLOCK. A majority (83 per cent) of the host galaxies have a catalogued redshift (shown in red). The hosts without a prior catalogued redshift (shown in blue), where the transient redshift was inferred from the classification spectrum, represent a fainter population of host galaxies.

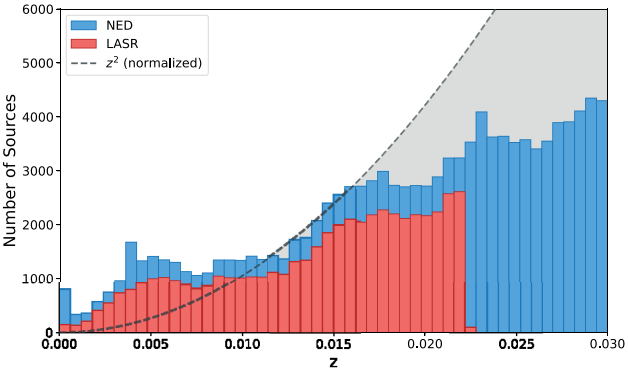

Figure 14. Histogram showing the redshift distribution of sources in the LASr (D. Asmus et al. 2020) and NED-LVS (D. O. Cook et al. 2023) catalogues within a redshift of 0.03. Since each redshift bin contains differential galaxy counts, we plot z^2 (dashed line) to represent the volume. z^2 is scaled to match the counts in the redshift bin at $z = 0.001$, since the local galaxy distribution at low redshift is dominated by the Local Group and Virgo Supercluster.

We also consider any other kinds of transients we may be missing within 100 Mpc. The possibilities for missing transients are:

(i) Very remote transients: unclassified transients with a projected separation higher than 50 kpc from their hosts (since if they were classified on the TNS, a redshift would be available).

(ii) Faint transients in faint hosts: unclassified transients in galaxies with no catalogued spectroscopic redshift. These hosts may either have been missed by spectroscopic programmes, or be too faint for multi-object surveys.

(iii) Classified transients with an error in the spectroscopic redshift of the host or the SN spectrum. The most likely are transients at the edge of the $z \leq 0.025$ limit which have a small error that places them beyond the cut.

To further quantify the missing fraction of transients in ATLAS100, we looked for bright, unclassified transients in ZTF BTS, that are not part of the ATLAS100 sample. The BTS has a very

high spectroscopic completeness (97 per cent) for bright transients with $m < 18$ mag (D. A. Perley et al. 2020). We find 40 transients in BTS within the relevant time window during 2017–2023, with a peak magnitude brighter than 17.5 mag, lacking a spectroscopic classification, and not already present in ATLAS100. The light curves and contextual information of these transients were examined, such as image stamps and host galaxy information to assess any genuine unclassified transients missing in our sample. We find five events that were classified as foreground CVs on the TNS, but the spectral type was not updated on BTS. 30 of these events show light curves and contextual information that is consistent with foreground CVs. We also find three nuclear transients that were likely AGN flaring activity. Finally, two events were known SNe within 100 Mpc and present in ATLAS100, but evaded the crossmatch due to duplicate TNS entries. Thus, the overwhelming majority of these transients are either confirmed or likely foreground CVs. We do not find any bright, unclassified transient in BTS missing in ATLAS100. The possibility of our sample missing intrinsically and apparently faint transients in galaxies that are also faint and lack redshift information remains. This should be addressed with LSST by Rubin and the 4MOST instrument that will measure galaxy redshifts to fainter limits than previously achieved combined with a systematic spectroscopic survey (TiDES; C. Frohmaier et al. 2025) of sources brighter than $m \lesssim 22$.

3.5.2 ATLAS100 and ZTF BTS

Most of the transients in our sample are equatorial or northern, with declination $\delta > -30^\circ$ (Fig. 3), given the later commissioning of the southern ATLAS units. We thus expect a significant overlap between the ATLAS100 and ZTF BTS samples. A cross-match yields only 441 transients in ATLAS100 that are also present in BTS. The BTS started on 2018 May 1, slightly later than ATLAS100. Even after accounting for 194 transients with $\delta < -30^\circ$ (limit for ZTF) and 119 transients that were discovered before 2018 May 1 in ATLAS100, the overlap (441 out of 1416, or 31 per cent) is still somewhat small. This is likely owing to the strict quality cuts on light curves imposed for BTS that remove nearly half their sample (D. A. Perley et al. 2020). To confirm, we checked the 975 transients in ATLAS100 that are missing in BTS, with discovery date after 2018 May 1 and $\delta > -30^\circ$. A majority (656 out of 975) were detected and registered to TNS by ZTF, but were excluded from the BTS sample due to the aforementioned quality cuts.

We also reviewed the demographics of the 975 transients missing from BTS, and whether they represent a similar or distinct population relative to the overall ATLAS100 sample. Of the 975 transients, 87 per cent are classified, identical to the overall sample. SNe II constitute 41 per cent and SNe Ia 31 per cent of the 975 missing objects, again identical to the overall ATLAS100 sample. This shows that the ATLAS100 transients missing from ZTF BTS constitute the same underlying population, and the BTS light curve quality cuts do not preferentially select for or against any transient type. ATLAS100 thus comprises a complementary data set with many objects not included in ZTF BTS. Although we do make quality cuts for fitting the light curves, we do not exclude any robustly identified transient within a redshift of 0.025, presenting a complete sample valuable for further investigation such as volumetric rate computations and global host galaxy properties.

3.5.3 Missed detections

A list of all transients reported to the TNS within the sample definition window, with a redshift of $z \leq 0.025$ was extracted and cross-matched with the ATLAS100 sample. We find 251 transients on TNS that are missing from our sample. This is attributable to several different factors noted below.

(i) Southern transients. The southern ATLAS units in Chile and South Africa were commissioned in late 2021, and became fully operational only by early- to mid-2022. The coverage in the south was quite patchy in the initial period following commissioning during early 2022. We thus missed southern transients with $\delta \leq -40^\circ$ that occurred before mid-2022. Out of the 251 transients, 70 were missed owing to the lack of southern sky coverage.

(ii) Faint transients. A fair number of faint transients, mostly discovered by ZTF and Pan-STARRS, were observed but peaked below the detection limit of ATLAS. Since these transients did not produce at least three 5σ detections in the difference images on any single epoch, they were not flagged and registered to the TNS and are thus missing from our sample. These account for 75 of the missing 251 transients.

(iii) Solar conjunction and gaps in coverage. Some missing transients are old SNe that emerged from solar conjunction, with declining light curves discovered well past peak. In other cases, the peak of the light curve was missed due to gaps in survey coverage, either due to weather or downtime. In both such events, the transients had faded below the detection limit of ATLAS by the time they were observable. These account for 23 of the missing transients.

(iv) Human error. In a small number of cases (5), the human scanner was not convinced by the veracity of the detection when presented with the difference images and forced photometry flux on the ATLAS transient science server marshall (K. W. Smith et al. 2020). These cases often involved faint transients detected just above the detection threshold, and/or transients located in proximity to the host galaxy nucleus or a bright foreground star. Because of the uncertainty, the transients were not promoted to the TNS and were instead placed in a 'possible' list awaiting further data for confirmation. In the remaining few cases the transient was not promoted due to human error or oversight.

(v) Genuine misses. Finally, we note a significant number (66) of transients that were observed by ATLAS and were brighter than typical ATLAS limiting magnitudes, as evidenced by their light curves from other surveys and forced photometry light curves retrieved from the ATLAS forced photometry server. As such these transients should have been flagged and promoted to the TNS, but were rejected during the data processing. Some of these transients were quite bright at peak and prompted us to investigate why they were missed. We find that they were detected by the PSF fitting routines by the ATLAS pipeline running on the images (producing the.ddc files as described in J. L. Tonry et al. 2018; K. W. Smith et al. 2020). A high fraction of these transients were nuclear or close to the core of a bright galaxy, resulting in a low initial real-bogus (RB) score from the machine-learning algorithm (K. W. Smith et al. 2020) when the transient was faint. The low RB score resulted in the transient being consigned to the 'garbage' list, and periodic purging of this list meant the candidate detection was discarded although subsequent detections from the rising transient were clearly significant. In other cases, SHERLOCK mistakenly identified and

labelled the transient as a variable star due to proximity with a foreground star. As part of the new routine operations of the ATLAS VRA, we now cross-match the garbage list with TNS once a week to identify potential misses, and whether they are from automated systems or human scanners. Since the ATLAS latitudes are well covered by other surveys such as ZTF and GOTO, this will eliminate misses of most transients, baring multiple algorithmic failures across independent systems, which is unlikely.

The remaining 12 objects had been previously vetted (Section 2.3) and rejected from the sample. These have a TNS object $z <= 0.025$, but either the identified SHERLOCK host has a catalogued redshift just over 0.025, or they are background impostors.

3.5.4 *Low luminosity transients*

For a limiting magnitude of $m_o \approx 19$, the ATLAS100 sample is complete within 100 Mpc for transients brighter than an absolute magnitude, $M_o \approx -16$. The sample is not complete at 100 Mpc for transients with intrinsically low luminosity, such as some faint SNe II (K. K. Das et al. 2024), faint SNe Iax (S. Srivastav et al. 2022), and several classes of gap transients like LRNe and ILRTs (V. R. Karambelkar et al. 2023). In addition to the intrinsic luminosity of the transient, several other factors may also affect the recovery efficiency including foreground Galactic extinction, host extinction, variations in survey sensitivity or 5σ limiting magnitude, gaps in sky coverage due to weather or technical downtime, galactocentric distance, and the element of human error. The galactocentric distance in particular seems to be an important factor as seen above in Section 3.5.3, since the higher level of noise in bright regions of the host galaxy affects the sensitivity, and image subtraction artefacts around bright galaxy cores also limit the discovery of fainter transients.

A forthcoming paper on luminosity functions and volumetric rates will present recovery efficiency simulations for different classes of transients in the sample using the ATLAS survey simulation tool (O. R. McBrien 2021). For a representative transient light curve as input, the code simulates a population of light curves distributed across a defined time window (taking into account survey history and sensitivity variations), sky coordinates (accounting for variations in Galactic extinction), and redshift within a defined volume, and performs an assessment of recovery (S. Srivastav et al. 2022; M. D. Fulton et al. 2025).

3.5.5 *Sample purity*

The classified transient sample is very pure due to the careful, manual checks on both the host galaxy associations and the classification spectra. We find no obvious systematic source of contaminants in those with a classification spectrum and would consider the classified sample as 100 per cent pure (in terms of being real transients). However, the classifications may be refined in the future with quantitative joint light curve and spectral analysis, so the classifications are not definitive even within the limitations of the qualitative classification scheme.

It is possible the unclassified subsample may have contaminants, although in Figs 5 and 8 the distributions of these compared to the classified SN sample are indistinguishable. There may be some in this sample which are background SN contaminants, lying beyond the 100 Mpc host but in chance alignment within the 50 kpc cross-match radius projected on to an angular radius. A background normal SN Ia at $z \approx 0.1$ will peak at $m_o \approx$ 19 mag, mimicking an intrinsically faint transient within 100 Mpc. In Section 2.3, we identified ∼60 background contaminants during the vetting process. It is possible that a small number ($\lesssim 10$) of faint, unclassified background transients persist in our final sample.

4 CONCLUSIONS

This paper presents the ATLAS 100 Mpc local volume survey (ATLAS100) sample of extragalactic transients within a redshift of $z \leq 0.025$ detected by the ATLAS survey during a span of 5.75 yr from 2017 September 21 to 2023 June 21. The sample definition and careful vetting process are described in detail, resulting in a total of 1729 transients, with hydrogen-rich SNe II and SNe Ia constituting the bulk (∼71 per cent) of the sample. The spectroscopic classification completeness is good, with 87 per cent of transients having at least one optical classification spectrum. We find a redshift completeness fraction for galaxies of 83 per cent within this volume. The sample is very pure, close to 100 per cent for spectroscopically classified supernovae and we estimate a very low contamination rate for the unclassified transients. The completeness depends on the absolute luminosities of the various transients and will be distance dependent, which will be addressed in future work. The light curves of all the transients that passed certain quality cuts were fit to extract peak luminosity and characteristic time-scale, defined as the time above half peak flux. We explore the statistical properties of the sample, including the demographics, host galaxy separations, and their location in the duration–luminosity diagram as a function of spectral type. This paper serves as a sample definition paper and marks the release of the catalogue and all light curve data, cleaned and binned into nightly data points.

ACKNOWLEDGEMENTS

We thank the anonymous referee for constructive comments that improved the quality of this paper.

This work has made use of data from the Asteroid Terrestrial-impact Last Alert System (ATLAS) project. The Asteroid Terrestrial-impact Last Alert System (ATLAS) project is primarily funded to search for near-Earth asteroids through NASA grants NN12AR55G, 80NSSC18K0284, and 80NSSC18K1575; byproducts of the NEO search include images and catalogues from the survey area. This work was partially funded by *Kepler/K2* grant J1944/80NSSC19K0112 and *HST* GO-15889, and STFC grants ST/T000198/1 and ST/S006109/1. The ATLAS science products have been made possible through the contributions of the University of Hawaii Institute for Astronomy, the Queen's University Belfast, the Space Telescope Science Institute, the South African Astronomical Observatory, and The Millennium Institute of Astrophysics (MAS), Chile and the University of Oxford.

This work is based (in part) on observations collected at the European Organisation for Astronomical Research in the Southern hemisphere, Chile as part of PESSTO, (the Public ESO Spectroscopic Survey for Transient Objects Survey), ePESSTO, and ePESSTO+ suveys.

SJS, SS, KWS, HFS, FS, AJC, and JHG acknowledge funding from the following grants held in Oxford: STFC Grant ST/Y001605/1, a Royal Society Research Professorship and Newton International Fellowship, a Schmidt AI in Science fellowship and the Hintze Family Charitable Foundation.

AC has been supported by the ANID, through grant ICN12_009 to the Millennium Institute of Astrophysics (MAS), and FONDECYT 1251692. AP acknowledges support from the PRIN-INAF 2022 'Shedding light on the nature of gap transients: from the observations to the models'. PR acknowledges support from STFC grant 2742655. LR acknowledges support from the Trottier Space Institute Fellowship and from the Canada Excellence Research Chair in Transient Astrophysics (CERC-2022-00009). T-WC acknowledges financial support from the Yushan Fellow Program of the Ministry of Education, Taiwan (MOE-111-YSFMS-0008-001-P1), and from the National Science and Technology Council, Taiwan (NSTC 114-2112-M-008-021-MY3).

MN, CRA, XS, and AA are supported by the European Research Council (ERC) under the European Union's Horizon 2020 research and innovation programme (grant agreement No. 948381).

DATA AVAILABILITY

The binned and cleaned ATLAS light curves for all transients in the sample are publicly available online on the Oxford Research Archive (https://ora.ox.ac.uk/objects/uuid:dbb60078-60ec-42af-8b50-53be5115de0a). The methods used for processing the light curve data are described in Section 2.5 and Appendix A. The data release includes a catalogue file containing additional details about the transients, including redshifts, distances, updated classifications, and host galaxy associations.

REFERENCES

Abbott B. P. et al., 2017, ApJ, 848, L12
Ackley K. et al., 2020, A&A, 643, A113
Alam S. et al., 2015, ApJS, 219, 12
Anderson J. P., James P. A., 2009, MNRAS, 399, 559
Andreoni I. et al., 2017, PASA, 34, e069
Angus C. R. et al., 2024, ApJ, 977, L41
Arcavi I. et al., 2016, ApJ, 819, 35
Asmus D. et al., 2020, MNRAS, 494, 1784
Ayala B. et al., 2025, A&A, 701, A128
Baltay C. et al., 2013, PASP, 125, 683
Barbary K. et al., 2025, SNCosmo, Zenodo, doi:10.5281/zenodo.15019859
Barna B. et al., 2021, MNRAS, 501, 1078
Bazin G. et al., 2009, A&A, 499, 653
Bellm E. C. et al., 2019, PASP, 131, 018002
Blagorodnova N. et al., 2017, ApJ, 834, 107
Blagorodnova N. et al., 2018, PASP, 130, 035003
Blagorodnova N. et al., 2021, A&A, 653, A134
Blondin S., Tonry J. L., 2007, ApJ, 666, 1024
Blondin S., Dessart L., Hillier D. J., Ramsbottom C. A., Storey P. J., 2023, A&A, 678, A170
Bolin B. T. et al., 2025, ApJ, 984, L25
Bostroem K. A. et al., 2023, ApJ, 956, L5
Botticella M. T. et al., 2009, MNRAS, 398, 1041
Botticella M. T. et al., 2017, A&A, 598, A50
Brennan S. J. et al., 2024, A&A, 684, L18
Brennan S. J. et al., 2025, preprint (arXiv:2503.08768)
Burgaz U. et al., 2025, A&A, 694, A9
Burke J. et al., 2021, ApJ, 919, 142
Cai Y. Z. et al., 2021, A&A, 654, A157
Cai Y. Z. et al., 2022, A&A, 667, A4
Callan F. P. et al., 2025, A&A, 702, A29
Cano Z., 2013, MNRAS, 434, 1098
Cao Y. et al., 2015, Nature, 521, 328
Cartier R. et al., 2026, A&A, 707, A161
Chambers K. C. et al., 2016, preprint (arXiv:1612.05560)
Chen P. et al., 2022, ApJS, 259, 53
Chen P. et al., 2024, Nature, 625, 253
Chen T.-W. et al., 2025, ApJ, 983, 86
Cold C., Hjorth J., 2023, A&A, 670, A48
Cook D. O. et al., 2023, ApJS, 268, 14
Dan M., Rosswog S., Brüggen M., Podsiadlowski P., 2014, MNRAS, 438, 14
Das K. K. et al., 2024, ApJ, 969, L11
Das K. K. et al., 2025a, PASP, 138, 024204
Das K. K. et al., 2025b, Transient Name Server AstroNote, 64, 1
Dastidar R. et al., 2025, A&A, 694, A260
De K. et al., 2020, ApJ, 905, 58
Desai D. D. et al., 2024, MNRAS, 530, 5016
Desai D. D. et al., 2026, preprint (arXiv:2602.00223)
DESI Collaboration, 2024, AJ, 168, 58
Dessart L., Hillier D. J., Livne E., Yoon S.-C., Woosley S., Waldman R., Langer N., 2011, MNRAS, 414, 2985
Dimitriadis G. et al., 2019, ApJ, 870, L1
Dimitriadis G. et al., 2023, MNRAS, 521, 1162
Dimitriadis G. et al., 2025, A&A, 694, A10
Dong Y. et al., 2024, ApJ, 977, 254
Drake A. J. et al., 2009, ApJ, 696, 870
Drout M. R. et al., 2014, ApJ, 794, 23
Dutta A. et al., 2022, ApJ, 925, 217
Elias-Rosa N. et al., 2024, A&A, 686, A13
Ertini K. et al., 2023, MNRAS, 526, 279
Ertini K. et al., 2026, preprint (arXiv:2602.03638)
Ferrari L. et al., 2024, MNRAS, 529, L33
Flewelling H. A. et al., 2020, ApJS, 251, 7
Foley R. J., 2015, MNRAS, 452, 2463
Foley R. J. et al., 2009, AJ, 138, 376
Foley R. J. et al., 2013, ApJ, 767, 57
Foley R. J. et al., 2018, MNRAS, 475, 193
Fraser M. et al., 2013, ApJ, 779, L8
Fremling C. et al., 2020, ApJ, 895, 32
Frohmaier C., Sullivan M., Maguire K., Nugent P., 2018, ApJ, 858, 50
Frohmaier C. et al., 2019, MNRAS, 486, 2308
Frohmaier C. et al., 2025, ApJ, 992, 158
Fulton M. D. et al., 2025, MNRAS, 542, 541
Gaia Collaboration, 2023, A&A, 674, A1
Gal-Yam A., 2017, Observational and Physical Classification of Supernovae. Springer International Publishing, Cham, p. 195
Galbany L. et al., 2020, Transient Name Server Classification Report, 2020-1561, 1
Gangopadhyay A. et al., 2020, ApJ, 889, 170
Gezari S., 2021, ARA&A, 59, 21
Gillanders J. H., Sim S. A., Smartt S. J., 2020, MNRAS, 497, 246
Gillanders J. H. et al., 2024, ApJ, 969, L14
Gomez S., Berger E., Nicholl M., Blanchard P. K., Hosseinzadeh G., 2022, ApJ, 941, 107
Groot P. J. et al., 2024, PASP, 136, 115003
Guy J. et al., 2007, A&A, 466, 11
Harutyunyan A. H. et al., 2008, A&A, 488, 383
Heinze A. N. et al., 2018, AJ, 156, 241
Heinze A. N. et al., 2021, PSJ, 2, 12
Hiramatsu D. et al., 2023, ApJ, 955, L8
Ho A. Y. Q. et al., 2019, ApJ, 871, 73
Ho A. Y. Q. et al., 2023, ApJ, 949, 120
Hoogendam W. B., Shappee B. J., Brown P. J., Tucker M. A., Ashall C., Piro A. L., 2024, ApJ, 966, 139
Hosseinzadeh G. et al., 2023, ApJ, 953, L15
Howell D. A. et al., 2005, ApJ, 634, 1190
Hung T. et al., 2021, ApJ, 917, 9
Ihanec N. et al., 2020, Transient Name Server AstroNote, 207, 1
Inkenhaag A., Jonker P. G., Levan A. J., Chrimes A. A., Mummery A., Perley D. A., Tanvir N. R., 2023, MNRAS, 525, 4042
Inserra C., 2023, in EAS2023, EAS Annual Meeting. p. 78
Irani I., Zimmerman E., Yaron O., Bruch R., 2020, Transient Name Server Classification Report, 2020-402, 1

Irani I. et al., 2024, ApJ, 962, 109
Ivanova N., Justham S., Avendano Nandez J. L., Lombardi J. C., 2013, Science, 339, 433
Ivezić Ž. et al., 2019, ApJ, 873, 111
Jacobson-Galán W. V. et al., 2020, ApJ, 898, 166
Jacobson-Galán W. V. et al., 2022a, ApJ, 924, 15
Jacobson-Galán W. V. et al., 2022b, ApJ, 932, 58
Jacobson-Galán W. V. et al., 2023, ApJ, 954, L42
Jencson J. E. et al., 2023, ApJ, 952, L30
Jha, S. W., 2017, in Handbook of Supernovae, ed. A. W. Alsabti & P. Murdin (Springer), 375
Jiang J.-a., Doi M., Maeda K., Shigeyama T., 2018, ApJ, 865, 149
Jiang J.-a. et al., 2021, ApJ, 923, L8
Kaiser N. et al., 2010, in Stepp L. M., Gilmozzi R., Hall H. J. eds, Proc. SPIE Conf. Ser. Vol. 7733, Ground-based and Airborne Telescopes III. SPIE, Bellingham, p. 77330E
Kangas T. et al., 2024, A&A, 689, A182
Karambelkar V. R. et al., 2021, ApJ, 921, L6
Karambelkar V. R. et al., 2023, ApJ, 948, 137
Karamehmetoglu E. et al., 2023, A&A, 678, A87
Kasen D., 2006, ApJ, 649, 939
Kasen D., 2010, ApJ, 708, 1025
Kasliwal M. M., 2012, PASA, 29, 482
Kilpatrick C. D. et al., 2023, ApJ, 952, L23
Kozyreva A., Janka H.-T., Kresse D., Taubenberger S., Baklanov P., 2022, MNRAS, 514, 4173
Kromer M. et al., 2013, ApJ, 778, L18
Kromer M. et al., 2016, MNRAS, 459, 4428
Kulkarni S. R. et al., 2007, Nature, 447, 458
Kulkarni S. R., Perley D. A., Miller A. A., 2018, ApJ, 860, 22
Kuncarayakti H. et al., 2023, A&A, 678, A209
Kwok L. A. et al., 2024, ApJ, 966, 135
Kwok L. A. et al., 2025, ApJ, 989, L33
Lach F., Callan F. P., Bubeck D., Röpke F. K., Sim S. A., Schrauth M., Ohlmann S. T., Kromer M., 2022, A&A, 658, A179
Law N. M. et al., 2009, PASP, 121, 1395
Levanon N., Soker N., 2017, MNRAS, 470, 2510
Li W. et al., 2011, MNRAS, 412, 1441
Li W. et al., 2019, ApJ, 870, 12
Lim G. et al., 2023, ApJ, 949, 33
Liu X.-L., Dou L.-M., Chen J.-H., Shen R.-F., 2022, ApJ, 925, 67
Lopez K. M., Kostrzewa-rutkowska Z., Yaron O., Knezevic N., 2017, Transient Name Server Classification Report, 2017-1332, 1
Lunnan R. et al., 2017, ApJ, 836, 60
Lyman J. D., Levan A. J., Church R. P., Davies M. B., Tanvir N. R., 2014, MNRAS, 444, 2157
Lyman J. D., Bersier D., James P. A., Mazzali P. A., Eldridge J. J., Fraser M., Pian E., 2016, MNRAS, 457, 328
Maeda K., Kuncarayakti H., Nagao T., Kawabata M., Taguchi K., Uno K., De K., 2026, PASJ, 78, L1
Magee M. R., Maguire K., 2020, A&A, 642, A189
Magnier E. A. et al., 2020, ApJS, 251, 6
Maguire K. et al., 2011, MNRAS, 418, 747
Maguire K. et al., 2023, MNRAS, 525, 1210
Malyali A. et al., 2024, MNRAS, 531, 1256
Margutti R. et al., 2019, ApJ, 872, 18
Marlin E. G. et al., 2025, preprint (arXiv:2512.21903)
McBrien O. R., 2021, PhD thesis, Queen's Univ. Belfast
McBrien O. R. et al., 2019, ApJ, 885, L23
McBrien O. R. et al., 2021, MNRAS, 500, 4213
Milisavljevic D. et al., 2017, ApJ, 846, 50
Miller A. A. et al., 2020, ApJ, 898, 56
Mockler B., Hammerstein E., Coughlin E. R., Nicholl M., in Encyclopedia of Astrophysics, 423, 3,
Modjaz M., Gutiérrez C. P., Arcavi I., 2019, Nat. Astron., 3, 717
Moore T. et al., 2023a, Transient Name Server AstroNote, 10, 1
Moore T. et al., 2023b, ApJ, 956, L31
Morán-Fraile J., Holas A., Röpke F. K., Pakmor R., Schneider F. R. N., 2024, A&A, 683, A44
Moran S. et al., 2024, A&A, 688, A161
Moriya T. J., Mazzali P. A., Ashall C., Pian E., 2023, MNRAS, 522, 6035
Mummery A., van Velzen S., Nathan E., Ingram A., Hammerstein E., Fraser-Taliente L., Balbus S., 2024, MNRAS, 527, 2452
Muthukrishna D., Parkinson D., Tucker B. E., 2019, ApJ, 885, 85
Newville M. et al., 2025, LMFIT: Non-Linear Least-Squares Minimization and Curve-Fitting for Python, Zenodo, doi:10.5281/zenodo.15014437
Nicholl M. et al., 2020, MNRAS, 499, 482
Nicholl M., Margalit B., Schmidt P., Smith G. P., Ridley E. J., Nuttall J., 2021, MNRAS, 505, 3016
Nicholl M. et al., 2023, ApJ, 954, L28
Nugent P., Kim A., Perlmutter S., 2002, PASP, 114, 803
Ofek E. O. et al., 2014, ApJ, 789, 104
Pakmor R., Kromer M., Taubenberger S., Sim S. A., Röpke F. K., Hillebrandt W., 2012, ApJ, 747, L10
Paniagua I. A. A. et al., 2026, ApJ, 997, 261
Pastorello A. et al., 2007, Nature, 447, 829
Pastorello A. et al., 2013, ApJ, 767, 1
Pastorello A. et al., 2019a, A&A, 625, L8
Pastorello A. et al., 2019b, A&A, 628, A93
Pastorello A. et al., 2021, A&A, 647, A93
Pastorello A. et al., 2023, A&A, 671, A158
Pastorello A. et al., 2025, A&A, 701, A32
Pearson J. et al., 2023, ApJ, 945, 107
Pellegrino C. et al., 2022a, ApJ, 926, 125
Pellegrino C. et al., 2022b, ApJ, 938, 73
Perets H. B. et al., 2010, Nature, 465, 322
Perley D. A. et al., 2019, MNRAS, 484, 1031
Perley D. A. et al., 2020, ApJ, 904, 35
Pessi T. et al., 2025, A&A, 703, A34
Pian E. et al., 2017, Nature, 551, 67
Piro A. L., Morozova V. S., 2016, ApJ, 826, 96
Podsiadlowski P., Joss P. C., Hsu J. J. L., 1992, ApJ, 391, 246
Polin A., Nugent P., Kasen D., 2019, ApJ, 873, 84
Prentice S. J. et al., 2018, ApJ, 865, L3
Prentice S. J. et al., 2019, MNRAS, 485, 1559
Pursiainen M. et al., 2018, MNRAS, 481, 894
Quimby R. M. et al., 2011, Nature, 474, 487
Raskin C., Kasen D., 2013, ApJ, 772, 1
Rau A. et al., 2009, PASP, 121, 1334
Reguitti A. et al., 2021, MNRAS, 501, 1059
Reguitti A., Pignata G., Pastorello A., Dastidar R., Reichart D. E., Haislip J. B., Kouprianov V. V., 2024, A&A, 686, A231
Rest S. et al., 2023, ATClean: High-Fidelity, Statistically Clean ATLAS Light Curves and Feature Detection, Zenodo, doi:10.5281/zenodo.7897346
Rest S. et al., 2025, ApJ, 979, 114
Rodríguez Ó., Nakar E., Maoz D., 2024, Nature, 628, 733
Sai H. et al., 2022, MNRAS, 514, 3541
Schuldt S., Vogl C., Taubenberger S., Fiore A., Benetti S., Cappellaro E., Tomasella L., Turatto M., 2019, Transient Name Server Classification Report, 2019-317, 1
Schulze S. et al., 2024, A&A, 683, A223
Seligman D. Z. et al., 2025, ApJ, 989, L36
Shappee B. J. et al., 2014, ApJ, 788, 48
Shappee B. J. et al., 2019, ApJ, 870, 13
Sharma Y. et al., 2023, ApJ, 948, 52
Sharma Y. et al., 2024, ApJ, 966, 199
Shen K. J., Quataert E., Pakmor R., 2019, ApJ, 887, 180
Shingles L. et al., 2021, Transient Name Server AstroNote, 7, 1
Shrestha M. et al., 2024, ApJ, 972, L15
Siebert M. R. et al., 2024, ApJ, 960, 88
Silverman J. M. et al., 2013, MNRAS, 436, 1225
Singh M. et al., 2024, ApJ, 965, 73
Sit T. et al., 2023, ApJ, 959, 142
Skrutskie M. F. et al., 2006, AJ, 131, 1163

Smartt S. J. et al., 2015, A&A, 579, A40
Smartt S. J. et al., 2017, Nature, 551, 75
Smartt S. J. et al., 2018, Astron. Telegram, 11727, 1
Smartt S. J. et al., 2024, MNRAS, 528, 2299
Smith K. W. et al., 2019, Transient Name Server AstroNote, 17, 1
Smith K. W. et al., 2020, PASP, 132, 085002
Smith N., 2014, ARA&A, 52, 487
Smith N., 2016, Interacting Supernovae: Types IIn and Ibn. Springer International Publishing, Cham, p. 1
Smith N., Li W., Filippenko A. V., Chornock R., 2011a, MNRAS, 412, 1522
Smith N., Li W., Silverman J. M., Ganeshalingam M., Filippenko A. V., 2011b, MNRAS, 415, 773
Sollerman J. et al., 2020, A&A, 643, A79
Sollerman J. et al., 2021, A&A, 655, A105
Srivastav S. et al., 2020a, ApJ, 892, L24
Srivastav S., Smartt S. J., McBrien O., Smith K. W., Young D. R., 2020b, Transient Name Server Classification Report, 2020-730, 1
Srivastav S. et al., 2022, MNRAS, 511, 2708
Srivastav S. et al., 2023a, ApJ, 943, L20
Srivastav S. et al., 2023b, ApJ, 956, L34
Srivastav S. et al., 2024, Transient Name Server AstroNote, 100, 1
Stalder B. et al., 2017, ApJ, 850, 149
Steeghs D. et al., 2022, MNRAS, 511, 2405
Steele I. A. et al., 2004, in Oschmann J. M., Jr ed., Proc. SPIE Conf. Ser. Vol. 5489, Ground-based Telescopes. SPIE, Bellingham, p. 679
Stevance H. F., Smith K. W., Smartt S. J., Roberts S. J., Erasmus N., Young D. R., Clocchiatti A., 2025, ApJ, 990, 201
Stritzinger M. D. et al., 2014, A&A, 561, A146
Strotjohann N. L. et al., 2021, ApJ, 907, 99
Szalai T. et al., 2024, A&A, 690, A17
Taddia F. et al., 2018, A&A, 609, A136
Taubenberger S., 2017, The Extremes of Thermonuclear Supernovae. Springer International Publishing, Cham, p. 317
Taubenberger S., Kromer M., Pakmor R., Pignata G., Maeda K., Hachinger S., Leibundgut B., Hillebrandt W., 2013, ApJ, 775, L43
Taubenberger S. et al., 2019, MNRAS, 488, 5473
Teja R. S. et al., 2023, ApJ, 954, 155
Terwel J. et al., 2021, Transient Name Server AstroNote, 50, 1
Tomasella L. et al., 2020, MNRAS, 496, 1132
Tonry J. L., 2011, PASP, 123, 58
Tonry J. L. et al., 2018, PASP, 130, 064505
Valenti S. et al., 2009, Nature, 459, 674
Valerin G. et al., 2022, MNRAS, 513, 4983
Valerin G. et al., 2025a, A&A, 695, A42
Valerin G. et al., 2025b, A&A, 695, A43
Villar V. A., Berger E., Metzger B. D., Guillochon J., 2017, ApJ, 849, 70
Villar V. A. et al., 2019, ApJ, 884, 83
Vincenzi M. et al., 2025, MNRAS, 541, 2585
Wang Q. et al., 2024, ApJ, 962, 17
Weston J. G., Smith K. W., Smartt S. J., Tonry J. L., Stevance H. F., 2024, RAS Techniques and Instruments, 3, 385
Wiseman P. et al., 2021, MNRAS, 506, 3330
Xi G. et al., 2024, MNRAS, 527, 9957
Xiang D. et al., 2024, ApJ, 969, L15
Yadavalli S. K. et al., 2024, ApJ, 972, 194
Yang S. et al., 2021, A&A, 655, A90
Yao Y. et al., 2022, ApJ, 937, 8
Yoon S.-C., Dessart L., Clocchiatti A., 2017, ApJ, 840, 10
Young D. R., 2023, Sherlock. Contextual classification of astronomical transient sources, Zenodo, doi:10.5281/zenodo.8038057
Zenati Y., Perets H. B., Dessart L., Jacobson-Galán W. V., Toonen S., Rest A., 2023, ApJ, 944, 22
Zimmerman E. A. et al., 2026, preprint (arXiv:2602.09096)

APPENDIX A: BASELINE CORRECTION

For each transient, the forced photometry was measured from difference images (Section 2.5). Occasionally, the reference wallpaper used for image subtraction contains some flux from the transient while it is still bright, resulting in underestimation of the true transient flux. To correct the photometric measurements for such cases, we compute a baseline flux correction for each transient light curve in the sample generated by ATCLEAN. This correction was computed using a pre-explosion window from -220 to -20 d relative to TNS discovery. The baseline correction was computed as a sigma-clipped median from the pre-explosion window. If the number of data points after sigma-clipping was insufficient for computing a robust correction ($N < 10$ for *o* band and $N < 5$ for *c* band), a late-time window from $+500$ to $+700$ d was used instead. The uncertainty on the correction was estimated using bootstrap resampling.

The baseline correction was only applied if it was at least 3σ significance, and the uncertainty on the offset was below 50 μJy. A significant baseline correction was computed and applied only to 275 light curves (246 unique transients) out of 3449 light curves (1729 unique transients). Most of these transients with a significant baseline correction were discovered during 2017–2019, when changes to the ATLAS reference wallpaper were more frequent. Overall, the applied corrections are generally small, with a median value of -26 μJy. Although a majority of these cases show negative baseline correction values, indicating the presence of positive transient flux in the reference image, a small number (47 out of 275) of light curves have positive (albeit small) baseline corrections. We note that there could be other sources of additional flux besides changes to reference images, such as AGN flaring activity in the host galaxy for nuclear transients, or a spatially coincident foreground variable star. Although this is a small effect in an overall sense, for individual transients we encourage users to adopt a custom baseline correction if required, and we thus include both the corrected and uncorrected data products.

Fig. A1 shows the ATLAS *o*-band light curve of SN 2017gmr as an example, with and without the offset correction. The uncorrected light curve shows a constant negative offset, indicating presence of SN flux in the reference image.

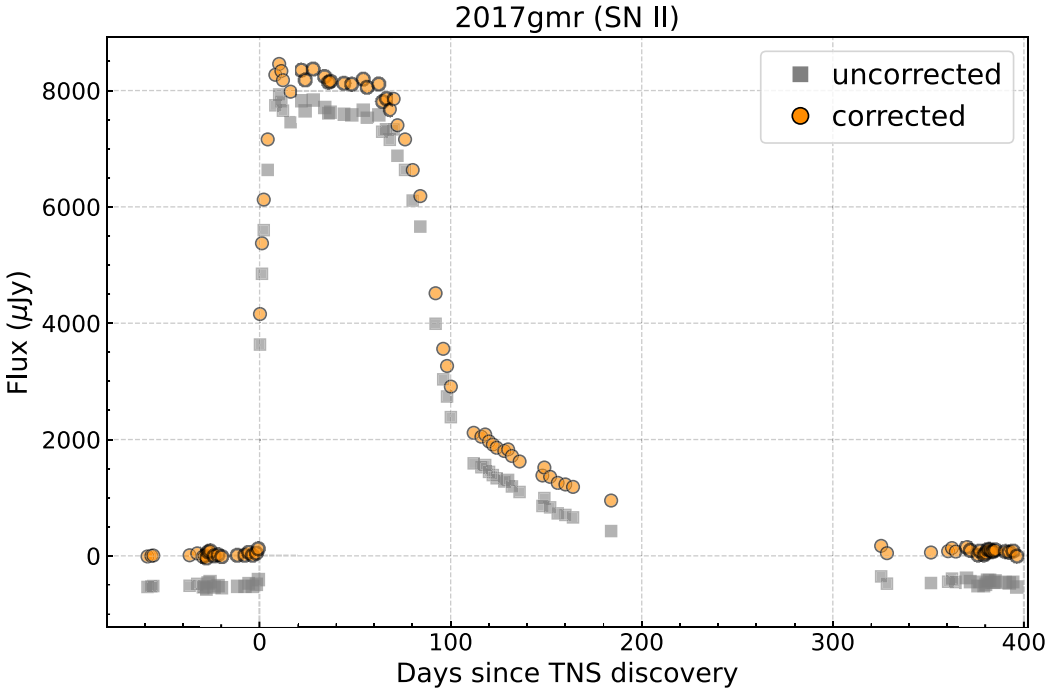

Figure A1. ATLAS *o*-band light curve of the type II SN 2017gmr, shown with (orange circles) and without (grey squares) the baseline correction. A correction of -524 ± 9 μJy was computed for SN 2017gmr from the pre-explosion window before TNS discovery.

[1]*Astrophysics, Department of Physics, University of Oxford, Denys Wilkinson Building, Keble Road, Oxford OX1 3RH, UK*
[2]*Astrophysics Research Centre, School of Mathematics and Physics, Queen's University Belfast, Belfast BT7 1NN, UK*
[3]*Space Telescope Science Institute, 3700 San Martin Dr, Baltimore, MD 21218, USA*
[4]*Graduate Institute of Astronomy, National Central University, 300 Jhongda Road, 32001 Jhongli, Taiwan*
[5]*INAF – Osservatorio Astronomico di Padova, Vicolo dell'Osservatorio 5, I-35122 Padova, Italy*
[6]*University Observatory, Faculty of Physics, Ludwig-Maximilians-Universität München, Scheinerstr 1, D-81679 Munich, Germany*
[7]*European Southern Observatory, Alonso de Córdova 3107, Casilla 19001, Santiago, Chile*
[8]*Institute for Astronomy, University of Hawai'i, 2680 Woodlawn Drive, Honolulu, HI 96822, USA*
[9]*Department of Physics and Astronomy, Johns Hopkins University, Baltimore, MD 21218, USA*
[10]*Trottier Space Institute at McGill, 3550 Rue University, Montreal, Quebec H3A 2A7, Canada*
[11]*Department of Physics, McGill University, 3600 Rue University, Montreal, Quebec H3A 2T8, Canada*
[12]*GSI Helmholtzzentrum für Schwerionenforschung, Planckstraße 1, D-64291 Darmstadt, Germany*
[13]*Department of Astronomy and Steward Observatory, University of Arizona, 933 North Cherry Avenue, Tucson, AZ 85721-0065, USA*
[14]*Instituto de Astrofisica, Pontificia Universidad Católica de Chile, Vicuña Mackenna, 4860 Macul, Santiago, Chile*
[15]*Instituto Milenio de Astrofisica (MAS), Nuncio Monseñor Sótero Sanz 100, Of. 104, Santiago, Chile*
[16]*South African Astronomical Observatory, Cape Town 7925, South Africa*
[17]*Department of Physics, Stellenbosch University, Stellenbosch 7602, South Africa*
[18]*Instituto de Alta Investigación, Universidad de Tarapacá, Casilla 7D, Arica, Chile*
[19]*School of Physics and Astronomy, University of Birmingham, Birmingham B15 2TT, UK*
[20]*Research School of Astronomy and Astrophysics, Australian National University, Canberra, ACT 0200, Australia*

This paper has been typeset from a TEX/LATEX file prepared by the author.